Development of cell-derived matrices for 3D *in vitro* cancer cell models.

Gerard Rubí-Sans, Agata Nyga, Elena Rebollo, Soledad Pérez-Amodio, Jorge Otero, Daniel Navajas, Miguel A. Mateos-Timoneda[*], *Elisabeth Engel*[*]

AUTHOR ADDRESS

Gerard Rubí-Sans - Institute for Bioengineering of Catalonia (IBEC), The Barcelona Institute of Science and Technology, Barcelona, Spain; CIBER en Bioingeniería, Biomateriales y Nanomedicina (CIBER-BBN), Barcelona, Spain.

Agata Nyga - Institute for Bioengineering of Catalonia (IBEC), The Barcelona Institute of Science and Technology, Barcelona, Spain.

Elena Rebollo - Molecular Imaging Platform, Molecular Biology Institute of Barcelona (IBMB-CSIC), Barcelona, Spain.

Soledad Pérez-Amodio - CIBER en Bioingeniería, Biomateriales y Nanomedicina (CIBER-BBN), Barcelona, Spain; Institute for Bioengineering of Catalonia (IBEC), The Barcelona Institute of Science and Technology, Barcelona, Spain; IMEM-BRT group, Department of Materials Science, EEBE, Technical University of Catalonia (UPC), Barcelona, Spain.

Jorge Otero - Unitat Biofísica i Bioenginyeria, Facultat de Medicina i Ciències de la Salut, Universitat de Barcelona, Barcelona, Spain; CIBER de Enfermedades Respiratorias, Madrid, Spain.

Daniel Navajas - Institute for Bioengineering of Catalonia (IBEC), The Barcelona Institute of Science and Technology, Barcelona, Spain; Unitat Biofísica i Bioenginyeria, Facultat de Medicina i Ciències de la Salut, Universitat de Barcelona, Barcelona, Spain; CIBER de Enfermedades Respiratorias, Madrid, Spain.

Miguel A. Mateos-Timoneda - Institute for Bioengineering of Catalonia (IBEC), The Barcelona Institute of Science and Technology, Barcelona, Spain; Bioengineering Institute of Technology, Universitat Internacional de Catalunya (UIC), Sant Cugat del Vallès (Barcelona), Spain.

Elisabeth Engel - Institute for Bioengineering of Catalonia (IBEC), The Barcelona Institute of Science and Technology, Barcelona, Spain; CIBER en Bioingeniería, Biomateriales y Nanomedicina (CIBER-BBN), Barcelona, Spain; IMEM-BRT group, Department of Materials Science, EEBE, Technical University of Catalonia (UPC), Barcelona, Spain.

KEYWORDS

3D Cell-derived matrices, extracellular microenvironment, microcarriers, adipose mesenchymal stem cells, macromolecular crowders, cytotoxicity assay

ABSTRACT

Most morphogenetic and pathological processes are driven by cells responding to the surrounding matrix, such as its composition, architecture, and mechanical properties. Despite increasing evidence for the role of extracellular matrix (ECM) in tissue and disease development, many *in vitro* substitutes still fail to effectively mimic the native microenvironment. We established a novel method to produce macroscale (>1 cm) mesenchymal cell-derived matrices (CDMs) aimed to mimic the fibrotic tumor microenvironment surrounding epithelial cancer cells. CDMs are produced by human adipose mesenchymal stem cells (hAMSCs) cultured in sacrificial 3D scaffold templates of fibronectin-coated poly-lactic acid (PLA) microcarriers (MCs) in presence of macromolecular crowders (MMCs). We showed that decellularized CDMs closely mimic the fibrillar protein composition, architecture, and mechanical properties of human fibrotic ECM from cancer masses. CDMs had highly reproducible composition made of collagen type I, III and fibronectin ECM with tunable mechanical properties. Moreover, decellularized and MCs-free CDMs were successfully repopulated with cancer cells throughout their 3D structure, and following chemotherapeutic treatment, cancer cells showed greater doxorubicin resistance compared to 3D culture in collagen hydrogels. Collectively, these results support the use of CDMs as a reproducible and tunable tool for developing 3D *in vitro* cancer models.

1. Introduction

The extracellular matrix (ECM) is a complex and heterogenous three-dimensional (3D) substrate produced by cells with which they actively interact through adhesion molecules [1–3]. In mammalian tissues, among many different molecules, ECM is composed of proteins (including collagen and elastin), glycoproteins (such as fibronectin or laminin), proteoglycans (as heparan sulphate or keratan sulphate) and growth factors (as VEGF, TGF-β), forming the interstitial connective tissue and the basement membrane [2–4]. ECM is tissue and organ specific and, besides structural support, it provides chemical and biomechanical cell signaling cues which drive cell behavior (i.e. polarity, migration, proliferation, differentiation and survival) responsible for tissue remodeling and maintenance [5–8], while its alteration can promote disease development [9,10]. Often, at the onset of a disease a dysregulation between the cell-ECM signaling interaction occurs leading to defects in the ECM assembly and cell metabolism [6,11]. As a consequence, these alterations trigger pathological changes in ECM composition, architecture and mechanical properties [12,13].

Cell-derived matrices (CDMs) provide a 3D cell culture strategy to recapitulate native microenvironment in vitro [14]. CDMs resemble biochemical, physical and mechanical properties of tissue microenvironment, providing a great alternative to decellularized tissues/organs or animal models [15]. Several methods are used to obtain CDMs, such as cell sheet cultures [16,17], cells seeded on top of electrospun fibers [18–20], microcarrier templates [21–23], and 3D printing [24] and bioprinting approaches [25]. CDMs can be produced using different cell sources, and repopulation can be done with cell types of choice, which allows to engineer specific tissue and disease *in vitro* models [26,27]. In addition, CDMs recellularization with patient's cells opens a door to develop patient-specific in vitro models as a personalized platform for drug screening and therapeutic target identification [28–30]. However, most of the mentioned methods produce CDMs as flat ECM sheets or microfabricated

patterns, with cells grown on top as a monolayer, a successful strategy used in skin regeneration or wound healing [31–38]. To provide a more complex 3D architecture, Chiang et al. used mesenchymal stem cell (MSC) spheroids to generate 3D CDMs, and shown successful repopulation with endothelial cells around the spherical shape [39]. However, the spherical CDMs reached a maximum size of 200 μm in diameter and required aggregation to form microtissues (~0.5-1 mm). Moreover, the cells did not grow throughout the spherical CDM scaffold but along its external surface.

Here, we describe 3D CDM scaffolds with tunable physical, biochemical and mechanical properties, mimicking the fibrotic ECM from human tumor microenvironment. We used biodegradable and biocompatible poly-lactic acid (PLA) microcarriers [23,24], which were previously shown to promote ECM deposition [21,40,41]. PLA microcarriers were coated with fibronectin and cultured with primary human adipose mesenchymal stem cells (hAMSCs), resulting in the production of macro size (>1 cm) complex matrices composed mainly of collagen type I, III, and fibronectin. The size, composition and stiffness were shown to be amendable by adding macromolecular crowders (MMCs) or through stirring culture.

As a proof-of-concept, CDMs were successfully repopulated throughout their structure with two different colorectal cancer cell lines (HT29 and SW480). A cytotoxicity assay using doxorubicin (dox) showed reduced response to dox of cells grown in CDMs compared to 3D collagen hydrogel matrices or 2D culture, resembling chemotherapeutic drug resistance observed in patients [42,43]. This highlights the drug resistance by providing a hard-to-penetrate barrier of biochemically and biomechanically complex matrix.

Altogether, our study provides a reliable and reproducible methodology to develop macro-sized CDMs for applications in cancer modelling.

2. Results and discussion

In this study, hAMSCs-seeded PLA microcarriers (MCs) are used as building blocks with an enhanced protein production by the addition of macromolecular crowders (MMCs) to obtain a complex and large 3D cell-derived extracellular matrix. The generation, optimization and characterization of this methodology resulted in a unique 3D CDM ready for translation into advanced *in vitro* cancer model and a drug screening tool.

2.1. Preliminary cell culture and biomaterial optimization

Firstly, we used MMCs to promote protein deposition, as shown previously in 2D cell cultures [44]. To determine the optimal MMCs concentration, we compared different ratios of MMCs (Table 2) in 2D cell cultures of hAMSCs and measured cell proliferation (Total DNA) and protein content (Total protein) (Fig. S1A-B). While different ratios of MMCs had no significant effect on hAMSCs proliferation, we observed difference in the protein content, with 18% v/v condition MMC leading to highest protein content (599.12 ± 41.34 µg/ml) when compared to control (C-, 450.38 ± 60.74 µg/ml). This ratio was selected for further experiments.

Secondly, we characterized the properties of MCs produced according to a method developed previously in our laboratory [45]. MCs in cell culture medium had a spherical shape (Fig. S2A-B) with average diameter of 109 ± 34.3 µm (Fig. S2C,F), and its 70% of size distribution (Fig. S2C,F) ranged from 70 to 120 µm. The heterogenous size distribution allows for production of CDMs with pores of various sizes promoting cell-attachment and proliferation. MCs were functionalized with fibronectin (Fig. S2D-E, green color), -a key ECM component involved in cell adhesion, migration and regeneration processes [46], and overexpressed in poor prognosis colorectal tumors [47]-, and seeded with hAMSCs. Up to 90% of MCs were successfully colonized by hAMSCs as

measured with the Microcarrier Colonization Rate percentage (%MCCR) with cell viability above 85% (Fig. S2G-I).

2.2. CDMs production and characterization

2.2.1. Microcarrier (MC) concentration

In order to establish efficient protocol for CDM production we tested different amounts of cell-seeded MCs (Table 1), including 3 mg (condition A), 5 mg (condition D) and 10 mg (condition E) over 21-day culture in presence of MMCs, and additional condition A supplemented with MCs (1.5 or 3 mg, condition B or C, respectively) on day 3, 7 and 14. Conditions A and D resulted in a successful production of CDMs, and further addition of MCs (conditions B and C) had no additive effect on CDM formation, but rather their accumulation on CDMs' surface (Fig. S3A-D). Condition E resulted in unstable CDMs with low construct integrity (Fig. S3E). High MCs concentration could lead to poor CDMs production through MCs overcrowding and limiting nutrient and oxygen diffusion [48,49].

DNA and protein content in CDMs from conditions A to D (Fig. 1A) were assessed with a PicoGreen assay and BCA assay, respectively. Significantly higher amounts of DNA were observed in condition D (2525.46 ± 484.82 ng/ml) compared to condition A (2190.93 ± 312.29 ng/ml). In contrast, there was no significant difference in protein content between condition D and A (Fig. 1B), indicating that the higher cell number in condition D, did not contribute to increase in protein deposition. On the other hand, addition of non-seeded MCs (conditions B 1069.85 ± 166.75 µg/ml, and C 886.71 ± 208.90 µg/ml) resulted in lower a protein content.

The expression of key extracellular matrix proteins (collagen type I (red) and type III (green)) was assessed using immunofluorescence (Fig. 1C). Protein deposition around MCs and cells was observed in z-stack images up to 200µm depth. SEM imaging showed CDM surrounding MCs'

surface (Fig. 1D). Interestingly, CDM was aligned on the sample's surface (Fig. 1D), while within the sample core CDM was misaligned (Fig. 1E). As observed by Harris et al., matrix alignment on the surface can be promoted by direct contact with cell culture medium, which stimulates cells to align and produce aligned ECM [50]. Moreover, morphological differences between CDMs' surface and core can also determine the alignment of CDM throughout their structure. Following 21 days of culture, cells proliferated more on CDMs' surface, as there were no space constraints (Fig. 1D). Cells deposited higher amounts of CDM which formed a dense crust of crosslinked protein fibers influencing surface ECM porosity (Fig. 1D). In consequence, spatially-homogenous protein deposition along the tissue was not achieved due to imbalanced diffusion of nutrients and oxygen towards internal parts (Fig. 1E). Moreover, condition D led to formation of largest 3D CDMs with length >1 cm and > 0.5 cm width (Fig. S3), which is between 2 to 3 times larger than previously reported [41]. Nevertheless, as conditions A and D, independently of the particle or cell number, led to a formation of tissues with the same protein content, similar morphology and high aggregation, we selected these conditions for further evaluation. This included cultures under static and stirring conditions to promote spatially-homogenous deposition of CDM on the outer and inner part of CDMs, under shorter cell culture time of 10 days.

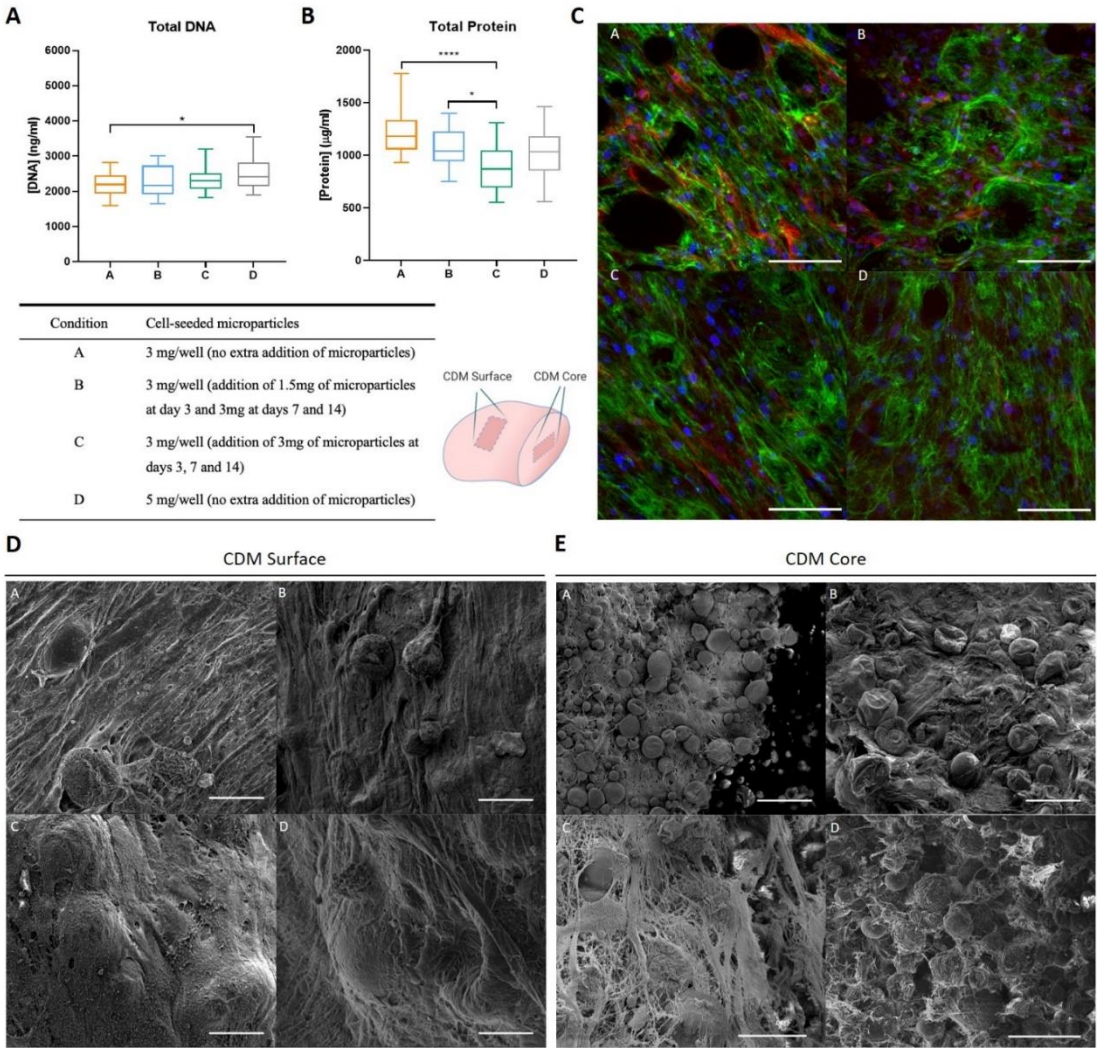

Figure 1 CDM production and characterization. Assessment of optimal microcarriers concentration after 21-day culture. **A** Total DNA, **B** Total protein determination. **C** Immunofluorescence staining of collagen types I (red), III (green) and DAPI (blue). Scale bars = 100µm. **D** SEM images of CDMs surface and **E** core topography. Scale bars: surface A, B, C and D = 50µm; core A, B and D = 200µm, C = 100µm. (Statistical differences: *p-value < 0.05, ****p < 0.0001, N = 3, n = 3, one-way ANOVA).

2.2.2. Static vs. Stirred cultures

Nutrients and oxygen diffusion allows for cell survival and growth in complex tissue structures [49,51], with their free diffusion limited to 200 μm [52]. Beyond this depth in lack of correct vasculature, the tissue structure can develop a necrotic core. To promote the diffusion of nutrients we used stirring cell culture conditions for condition A (3 mg) and D (5 mg) cultured with MMCs and compared them to static cultures. Following 10 days of culture, DNA content was significantly higher in stirred-condition D (5558.07 ± 580.10 ng/ml, Fig. 2A) than in the static-condition D (4835.27 ± 675.09 ng/ml), and cell viability qualitatively increased, as observed in live/dead CDM images (Fig. S4B,D). Similar results were observed when comparing the stirred- and static-condition A (Fig. S4A,C). This indicates that stirring promotes cell proliferation. Together with higher cell number, stirred-condition D resulted in the highest protein deposition (973.50 ± 133.74 μg/ml, Fig. 2B) reaching already similar protein deposition levels as observed after 21 days of static culture (1021.77 ± 217.69 μg/ml, Fig. 2B). Moreover, CDM formed after 10 days of culture displayed an aligned pattern on CDMs' surface (Fig. S5A), whereas within its core it was misaligned (Fig. S5B). The presence of collagen type I and type III (Fig. 2C) was confirmed in all static and stirred conditions after 10-day culture. Together, condition D was chosen for further experiments due to its higher protein deposition, DNA content, and its macroscale size, providing a true 3D microenvironment to generate *in vitro* cancer model.

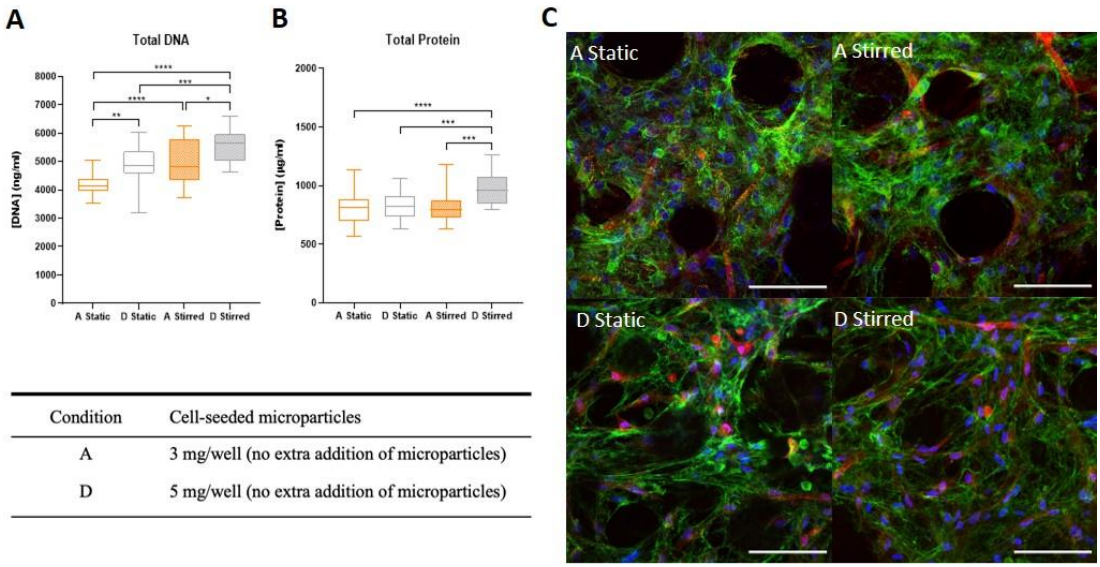

Condition	Cell-seeded microparticles
A	3 mg/well (no extra addition of microparticles)
D	5 mg/well (no extra addition of microparticles)

Figure 2 CDM production and characterization. Static vs. stirred cultures after 10-day culture. A Total DNA, **B** Total protein determination. **C** Immunofluorescence staining of collagen types I (red), III (green) and DAPI (blue). Scale bars = 100µm. (Statistical differences: *p-value < 0.05, **p < 0.01, ***p < 0.001, ****p < 0.0001, N = 3, n = 3, one-way ANOVA).

2.3. Gene expression in CDMs

The spatially-heterogenous extracellular matrix has tissue-dependent properties, including biochemical composition, physical organization and mechanical properties [5,7]. Matrix proteins are one of the main components of ECM, their absence or presence, together with the expression levels, are crucial for cell stimulation and response[7], and tissue development [4]. To understand the contribution of MMCs on the production of CDMs, we compared the CDMs with and without MMCs following 10-day culture. CDMs biochemical properties were assessed by gene expression quantification of four key proteins present in native ECM: collagen type I and type III -two fiber forming proteins with key structural properties-, collagen type IV -the main collagen component of the basement membrane separating tissue compartments-, and fibronectin -a key extracellular matrix protein involved in cellular adhesion, growth and migration [53,54].

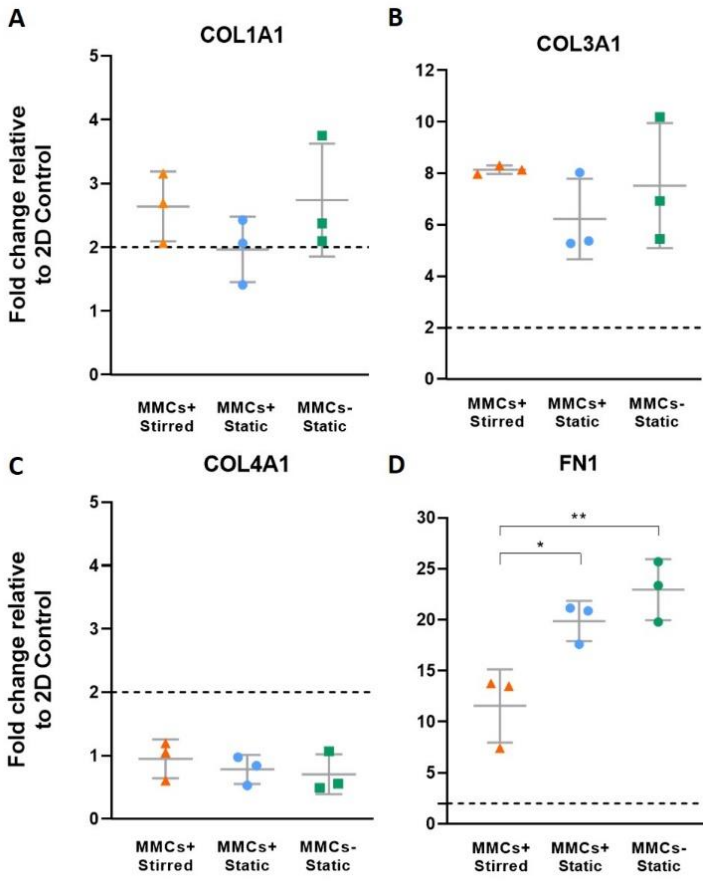

Figure 3 CDMs gene expression of key ECM proteins. A Collagen type I (COL1A1), **B** Collagen type III (COL3A1), **C** Collagen type IV (COL4A1) and **D** Fibronectin (FN1) gene expression was determined through qRT-PCR. Ct values relative to human beta actin (ACTB) were obtained and reported as fold increase (ΔΔCt) relative to 2D cultures. (Statistical differences: *$p < 0.05$, **$p < 0.01$, $N = 3$, $n = 3$, one-way ANOVA).

We measured the gene expression using condition D: MMCs+ Stirred, MMCs+ Static and MMCs- Static. MMCs- stirred condition was initially included in the study, however, lack of MMCs during stirring resulted in CDMs with an insufficient degree of aggregation and integrity. For this reason, MMCs- stirred CDMs were not further assessed in this study.

The mRNA expression of collagen type I (COL1A1) was significantly increased in MMCs+ Stirred (2.64 ± 0.55-fold change) and MMCs- Static (2.74 ± 0.89-fold change) conditions compared to cells cultured in 2D without MMCs (Fig. 3A). MMCs+ Static condition increased COL1A1 expression by 1.97 ± 0.51-fold change compared to 2D control (Fig. 3A). No significant differences were found between the tested conditions. Collagen type IV (COL4A1) mRNA levels were not changed when compared to 2D controls, suggesting that its genetic expression was not affected by the 3D cell adhesions or biomechanical properties provided by this culture strategy (Fig. 3C) [55]. On the other hand, collagen type III (COL3A1) and fibronectin (FN) mRNA expression were significantly increased in all tested conditions (increase ranging from 6.23 ± 1.56 to 8.14 ± 0.17-fold change in COL3A1) when compared to 2D controls (Fig. 3B,D). Significant differences in FN expression were found between MMCs+ Stirred (11.57 ± 3.59-fold change) compared to both MMCs+ Static (19.89 ± 1.97-fold change) and MMCs- Static (22.95 ± 2.98-fold change), suggesting that stirring conditions have a major impact on fibronectin gene expression within CDMs structure, as seen previously by Zhao and collaborators [56].

Overall, 3D CDM culture conditions significantly increased mRNA expression levels of collagen types I, III and fibronectin, while fibronectin expression was further increased in static conditions. Moreover, the presence of MMCs in static conditions had no major impact on gene expression of ECM proteins, further confirming that MMCs do not impact the cell signaling responses. These results suggest that the increased medium diffusion through stirring can impact the gene protein expression in matrix producing cells, similarly to previously reported effect caused by shear stress [57].

2.4. Cells and microcarriers removal from CDMs

Following initial CDMs characterization, condition D under stirred and static conditions were selected for further evaluation. To characterize CDMs' biochemical and mechanical properties, cells and MCs were removed from the whole construct using chemical and enzymatic digestions. To test the efficacy of cell and particle removal, and to quantify the potential loss of matrix from the CDMs, total DNA and protein were quantified. Total DNA results showed a 99.49 ± 0.14% reduction in DNA content in D stirred condition and a 98.65% ± 0.21% in D static, confirming nearly complete cell removal (Fig. 4A). CDM decellularization was also confirmed by immunofluorescence staining following decellularization (Fig. 4C) and MCs removal (Fig. 4D). No cells in CDMs were observed following both processes. Total protein analysis showed a significant reduction by 40.75 ± 0.05% in D stirred condition, while in D static conditions by 23.19 ± 0.12% (Fig. 4B). Therefore, the amount of protein after decellularization and MCs removal was 576.79 ± 78.66 µg/ml in D stirred and 634.61 ± 34.11 µg/ml in D static conditions (Fig. 4B). We expected this protein loss due to cell removal (intercellular protein loss), together with the removal of protein coating from PLA MCs.

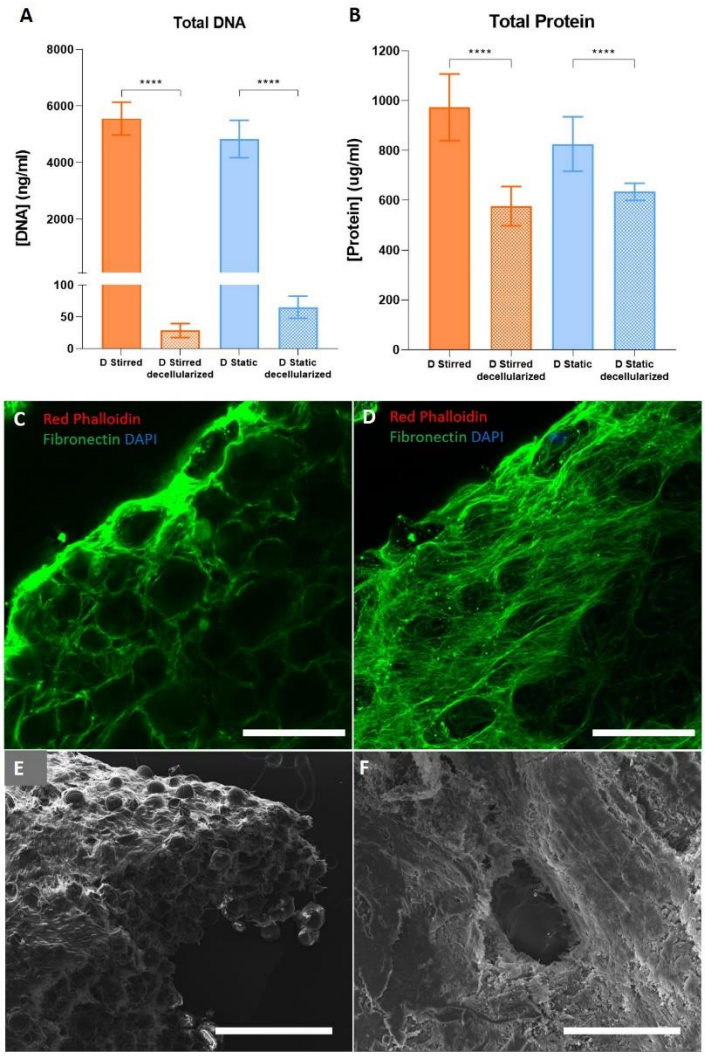

Figure 4 CDM decellularization and microcarriers removal after 10-day culture period. A Total DNA and **B** Total protein determination analysis after decellularization and MCs removal; D stirred condition (orange), D static condition (blue). **C** CDM immunofluorescent staining after decellularization and **D** MC removal, (Fibronectin (green), Red phalloidin (red) and DAPI (blue)) scale bars = 200 µm. **E** SEM image after decellularization. Scale bar = 500µm. **F** SEM image after MCs removal. Scale bar = 100µm. (Statistical differences: ****p-value 0.0001, N = 3, n = 3, one-way ANOVA).

SEM imaging confirmed the absence of MCs in CDMs after a chemical degradation process (Fig. 4F), when compared to CDMs after decellularization (Fig. 4E). Moreover, SEM images (Fig. 4F) showed that tissue integrity remained stable with empty pores where MCs were located. Decellularized and particle-less CDMs were compared to the samples prior to cell and MC removal through SEM microscopy (Fig. S5). Altogether, no structural or architecture qualitative differences were observed between samples before and after the decellularization and MCs removal, suggesting that CDMs integrity was not affected by these processes.

2.5. CDM protein composition characterization and quantification

Following decellularization and particle removal, the obtained CDMs were characterized for matrix protein composition, including collagen types I, III, IV and fibronectin using immunofluorescence staining (Fig. 5A-D). Based on the obtained images, we developed a protein quantification method using ImageJ [58] for automatic quantification of each image based on the fluorescence intensity. We used fluorescent images of protein standards using DOT blot method to correlate the fluorescence intensity with protein concentration.

Collagen type I, the most abundant protein in human tissues, was most expressed in the CDMs from all the conditions tested (Fig. 5A), with no significant differences between them. Fibronectin was the second most abundant protein in the MMCs+ CDMs, with similar levels in the different conditions tested. In contrast, in MMCs- CDMs, collagen III was the second most abundant protein. Finally, under static condition, presence of MMCs decreased the level of collagen type III while it increased deposition of collagen type IV (Fig. 5A). This suggests that MMCs supplementation specifically promote collagen type I and IV deposition. Measurements of collagen type I showed high standard deviation between samples, which corresponds to the heterogenous structure of CDMs, as seen in native ECM.

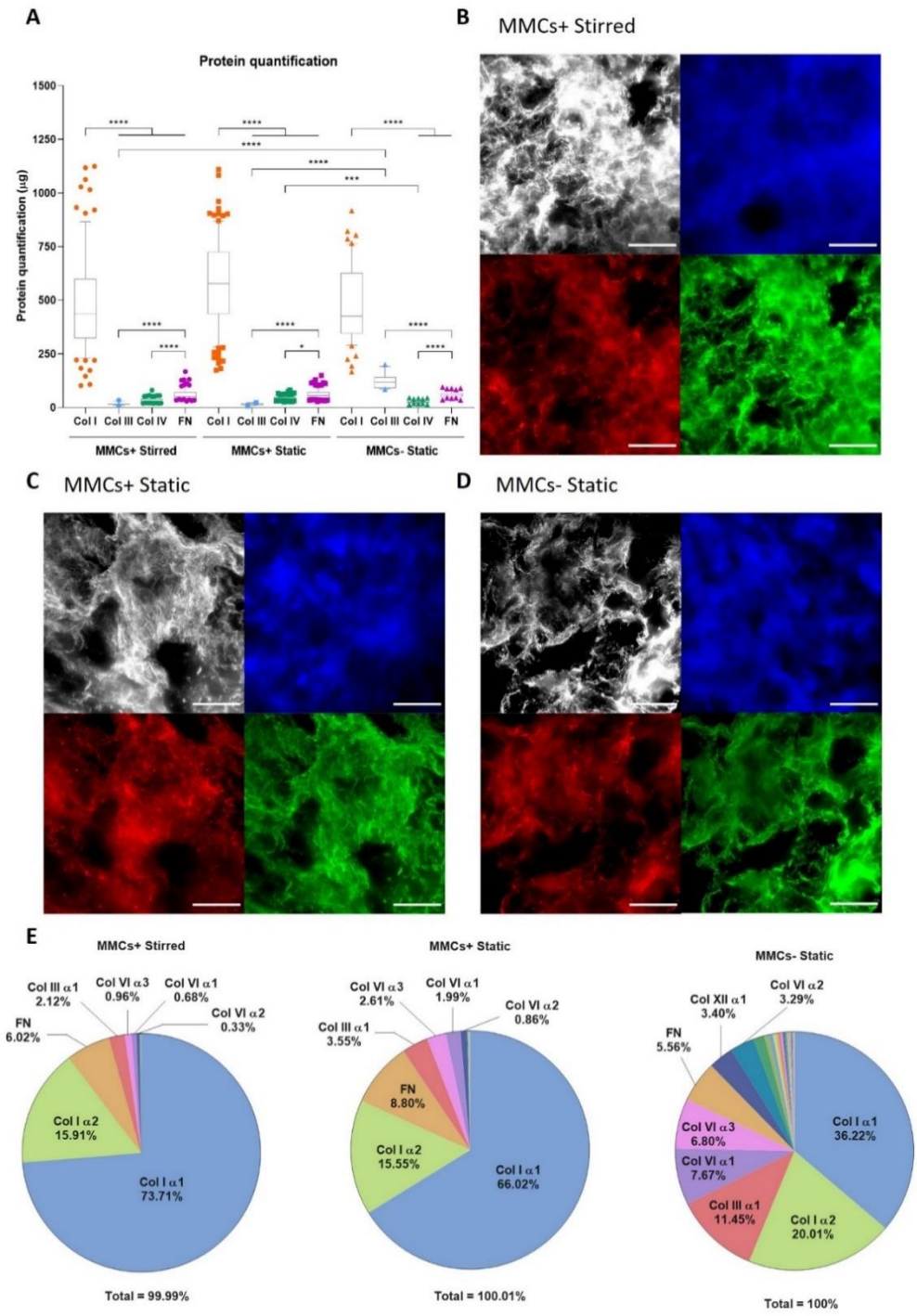

Figure 5 CDM protein composition and quantification. **A** Collagen type I, III, IV and fibronectin quantification results. **B-D** CDM immunofluorescence images for protein quantification, collagen type I (gray), III (blue), IV (red) and fibronectin (green), scale bars = 50 µm. **E** CDM protein composition assessment through mass spectrometry, percentual

quantification. (Statistical differences: *p < 0.05, ***p < 0.001, ****p < 0.0001, N = 3, n = 3, one-way ANOVA).

Next, mass spectrometry analysis was carried out to obtain a complete picture of the ECM proteins present in CDMs and validate results from immunofluorescence protein quantification (Fig. 5E). All proteins identified using mass spectrometry are listed in Table S1. Collagen family extracellular matrix proteins such as collagen types I, II, III, V, VI, XII, XVI and XVIII were found in all tested conditions.

Percentage protein quantification highlighted collagen type I as the most abundant protein in the three tested conditions (from 56.22% to 89.62% combining α1 and α2 subunits). However significant differences were found between MMCs- static condition (56.22%), MMCs+ stirred (89.62%) and MMCs+ static (81.68%), demonstrating that collagen I deposition and maturation is enhanced by the presence of MMCs, which were previously shown to alter cellular protein expression profiles [59]. MMCs increase collagen type I deposition and maturation via the increase in procollagen C-proteinase (PCP/BMP-1) and the proteolytic modification of its allosteric regulator, PCOLCE1 [60]. Following collagen type I, fibronectin was the second most abundant protein in MMCs+ stirred (6.02%) and MMCs+ static (8.80%) samples, with slightly reduced levels found in MMCs- static (5.56%) sample. However, in the MMCs- static condition, the expression of collagen III (11.45%), collagen VI α1 (7.67%) and α3 (6.80%) subunits were increased. This suggests that the presence of MMCs can alter cellular protein expression profile, as seen in the overexpression of collagen I. Instead, in the absence of MMCs, collagen type I is not upregulated, which also results in a higher collagen III content and overall higher percentages of other ECM proteins, as observed in mass spectrometry results. Interestingly, collagen type IV peptides were not found in MMCs+ Stirred condition, with low amounts in MMCs+ static

(0.005%) and MMCs- static (0.134%), whereas we observed positive expression using immunofluorescence protein quantification assay. This could be due to the CDM processing for mass spectrometry analysis or incorrect collagen IV peptide sequences. The presence of these four key ECM proteins in the generated CDMs confirms that these effectively recapitulate the composition of in vivo tissues such as connective or epithelial ones [2–4].

In summary, obtained results with this simple in-house developed method, allowed the quantification of ECM protein from immunostained sections. These results highly correlate with CDM mass spectrometry analysis, as similar protein proportions were found for the four studied ECM proteins, which validates the proposed method. As a result, we obtained a collagen-rich matrix produced by hAMSCs cells and composed mainly of collagen type I, and key ECM proteins such as collagen types III, IV and fibronectin among others found in smaller amounts. MMC- static CDMs' contained diverse ECM composition, which makes an alternative matrix source for generation of *in vitro* models of soft tissues (i.e., intestine, liver, kidneys or brain) [61–64]. Instead, MMCs+ CDMs (in static or stirred conditions), display a more fibrotic composition closer to cancer microenvironments, or collagen type I-rich tissues such as skin or muscle [65,66].

Together, our results indicate that the produced CDMs' biochemical complexity matches other commercial *in vitro* products, such as animal and/or tumor-derived Matrigel or Geltrex (made of laminin, collagen IV, heparin sulphate and enactin) [67], which makes our CDMs a great amendable substitution for 3D cell cultures.

2.6. CDM micromechanical properties

Micromechanics of the CDMs were measured using AFM, which is commonly accepted as the best-suited tool for testing the mechanical properties of the sample in the length scale (~1μm) at which cells sense their microenvironment [68]. Moreover, it was previously shown that freeze-

thawing for sample sectioning does not modify the mechanical properties of the extracellular matrix following decellularization [69]. Our results suggest that CDMs from MMCs+ Static condition are significantly stiffer (2565 ± 2008 Pa) than MMCs+ Stirred (1569 ± 1294 Pa) (Fig. 6). No significant differences were observed between MMC+ and MMC- static conditions, confirming that the addition of MMCs in the culture media do not affect the CDMs stiffness as observed previously with 3D scaffolds [70]. The softer CDMs in stirred condition correlate to the lower protein content measured after decellularization and MCs removal, and to reduced fibronectin deposition due to the increased media flow throughout the CDMs. On the other hand, reduced nutrient and oxygen diffusion throughout CDMs under static conditions enhanced the deposition of a thicker, denser and, therefore, stiffer CDM on the surface. Changes in the CDM composition can affect their micromechanical properties, as shown previously that the presence of fibronectin, collagen III and VI affect the collagen I fiber organization and matrix formation [71,72]. These changes in the matrix composition observed in our static and stirred cultures (especially related to fibronectin content), may result in the differences in CDM stiffness.

Nevertheless, observed differences in CDMs' stiffness provide an opportunity to tailor their use for stiffness-dependent tissue microenvironment, where CDM's mechanical properties can spontaneously guide cell recruitment, proliferation or differentiation processes [14,73–76]. CDM stiffness could be controlled by modifying MMCs concentration, as well as combining two or more crowding agents affecting different proteins' deposition and crosslinking [77–79], to better mimic microenvironment of tissues of choice.

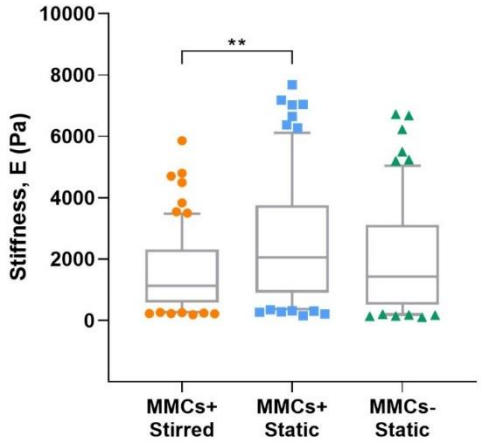

Figure 6 CDM micromechanical properties. (Statistical differences: **p < 0.01, N = 3, n = 3, one-way ANOVA)

2.7. Doxorubicin cytotoxicity assay

Following CDMs characterization, a proof-of-concept cancer viability assay was performed using CDMs from MMCs+ static condition which, as described above, had a fibrotic matrix (rich in collagen types I, III and fibronectin) with increased matrix stiffness that mimics the *in vivo* tumor stromal microenvironment [80–83]. Selected CDMs had an average length of 10.12 mm, width 5.17 mm, thickness 0.26 mm and 0.57 mg dry weight. Two epithelial colorectal adenocarcinoma cell lines, HT29 and SW480, were seeded in CDMs for 7 days. Following CDM repopulation, cells in CDMs were treated with increasing concentrations of doxorubicin (dox) (0, 0.5, 1 and 5 µM, similar *in vitro* concentrations to previously reported [84,85]) for a total period of 120 hours with cell viability measured after 24, 72 and 120 hours. Cell viability was normalized to control cells (0µM dox) at 24 hours. Reseeded CDMs were compared to two well established cell culture models: 2D cell cultures and 3D collagen type I gels of HT29 and SW480 cells, cultured in presence of MMCs. Both collagen type I gels (gel stiffness ≈ 1.6 kPa) and CDMs (CDM stiffness ≈ 2.5kPa) were within the range of colon tissue stiffness (0.9-4.4 kPa [86,87]). In addition, reseeded

CDMs showed cell penetration and migration within their structure, resembling a true 3D microenvironment (Fig. S6).

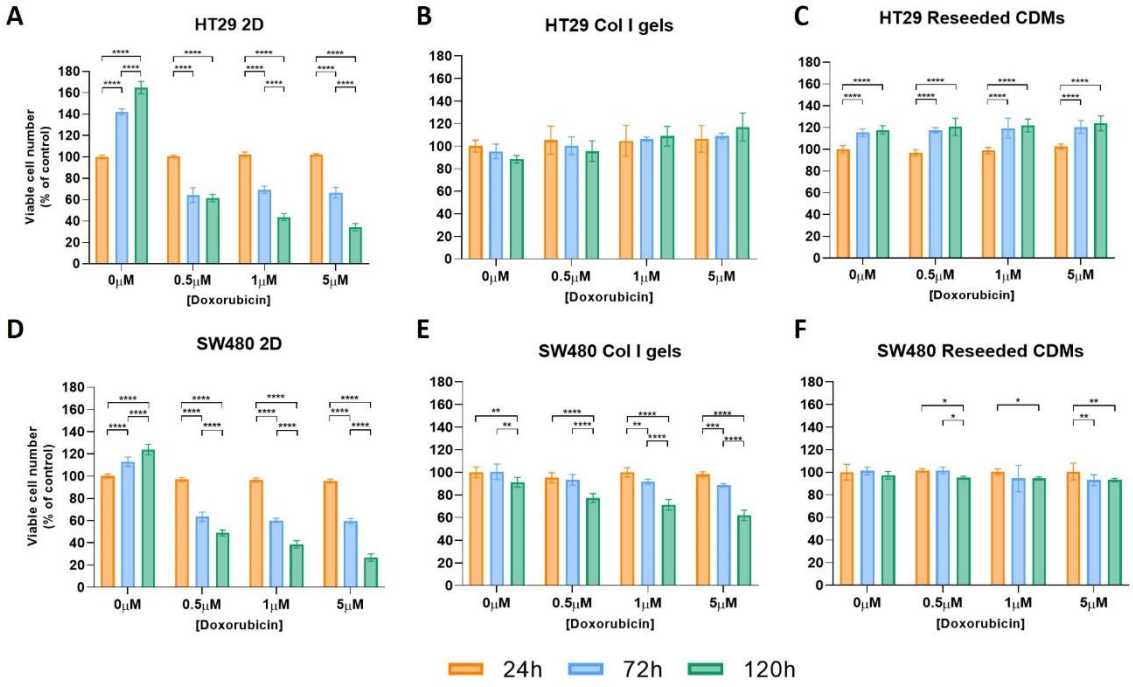

Figure 7 Doxorubicin cytotoxicity assay, cell viability. HT29 and SW480 colorectal cancer cell lines seeded in 2D (**A, D**), Collagen type I gels (**B, E**) and reseeded in CDMs (**C, F**). Statistical differences: *p-value < 0.05, **p < 0.01, ***p < 0.001, ****p < 0.0001, N = 3, n = 3, two-way ANOVA).

CDMs reseeded with HT29 showed increase in cell viability over time, while SW480 remained at stable level. When both cell lines cultured in 2D were treated with dox, their viability significantly decreased over time in a concentration-dependent manner (Fig. 7A,D). After 120 hours of treatment, both cell lines reached the half maximal inhibitory concentration (IC50) of dox at 1 μM and above, suggesting 1 μM as the minimum concentration needed to reduce cell viability at 50%.

HT29 cultured in 3D collagen type I gels did not respond to dox treatment throughout the 120-hour testing period (Fig. 7B). Similar lack of response to dox was observed in HT29 cultured in CDMs suggesting resistance to treatment in 3D microenvironments (Fig. 7C). SW480 cells embedded in Collagen type I gels showed a significant decrease in viability over time (Fig. 7E) in a concentration-dependent manner with a 30% and 40% reduction after 120 hours in presence of 1 and 5 μM of dox. Instead, in SW480 reseeded CDMs (Fig. 7F), cell viability decreased between 5.5% and 7% in the presence of dox, showing a lack of response to this chemotherapeutic drug.

CDMs' complex structure with specific biochemical, physical and mechanical properties provide cancer cells with microenvironment reducing dox distribution or promoting their resistance through cell-matrix signaling. These results suggest that CDMs can mimic the chemotherapeutic inefficacy in reaching and killing tumor masses in complex microenvironments. In addition, these results highlight the need for improved drug delivery methods and development of combinatory treatments to also disrupt the tumor-associated ECM.

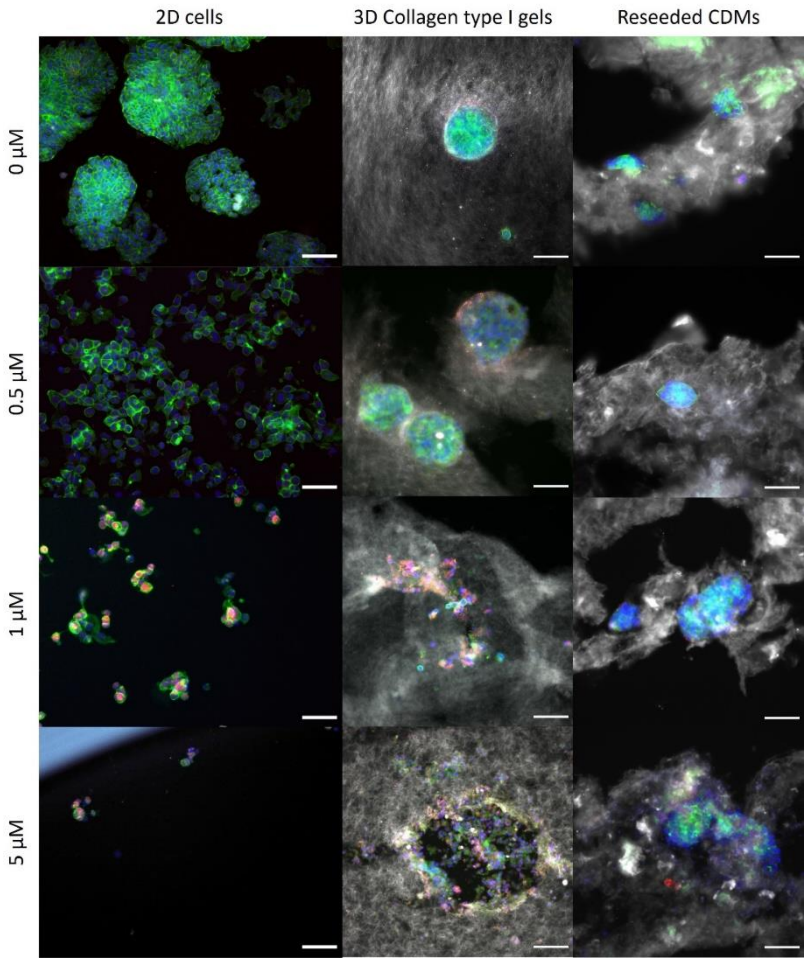

Figure 8 Doxorubicin cytotoxicity assay, immunofluorescence staining. HT29 colorectal cancer cell lines seeded in 2D, Collagen type I gels and reseeded in CDMs. Annexin V apoptosis marker (red), green phalloidin (green) and DAPI (blue). Scale bars = 100 µm.

Cell viability, morphology, and the expression of annexin V marker for cell apoptosis were assessed by immunofluorescence staining following 120 hours of dox treatment (Fig. 8). Annexin V expression (in red) increased with increasing concentrations of dox in 2D cultures, together with disruption to cell morphology. In 3D collagen gels, HT29 formed spheroid structures, which were disrupted at higher dox concentrations (1-5 µM). HT29 spheroids were also observed in reseeded CDMs, but their structure was preserved in presence of dox. Therefore, both 3D structures (collagen I gels and CDMs) can successfully recapitulate microenvironment for HT29 cells to

promote their growth as non-invasive spheroids, similar to structures observed in human tumors [88]. The lack of disruption to HT29 spheroids by dox in CDMs suggests the important role of the ECM composition in preventing drug permeability and, therefore, cell death [89].

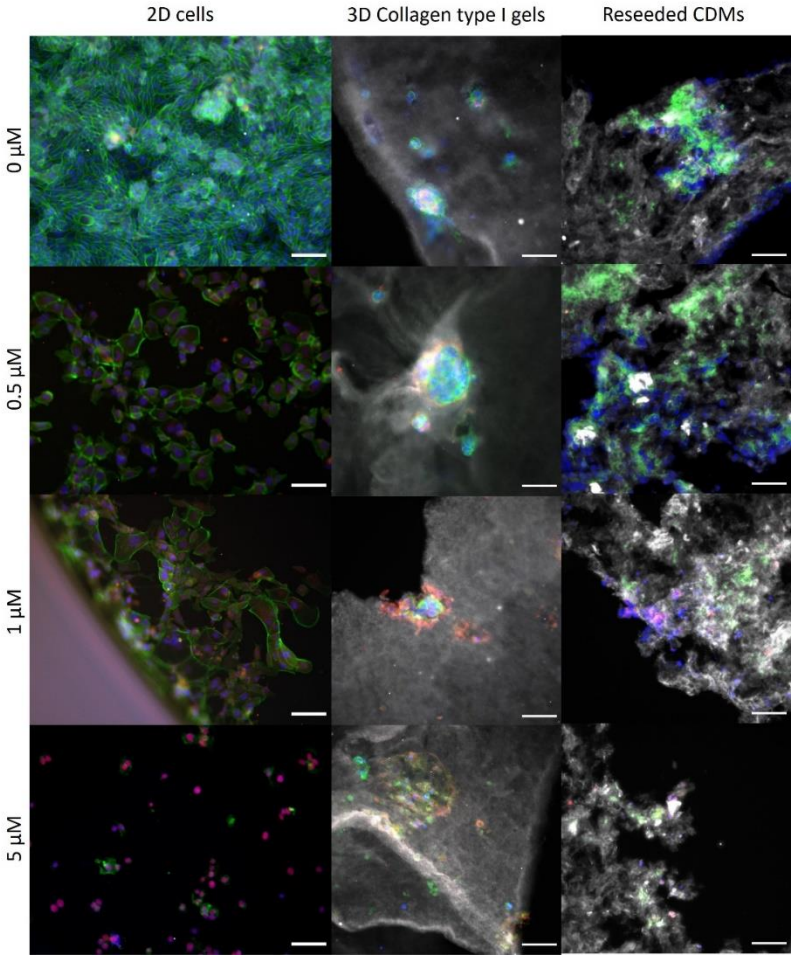

Figure 9 Doxorubicin cytotoxicity assay, immunofluorescence staining. SW480 colorectal cancer cell lines seeded in 2D, Collagen type I gels and reseeded in CDMs. Annexin V apoptosis marker (red), green phalloidin (green) and DAPI (blue). Scale bars = 100 µm.

SW480 cells (Fig. 9) in 2D culture showed decreased viability with increasing dox concentrations. Non-viable cells in presence of dox (0.5 - 5 µM) detached from substrate and were consequently removed during media changes. Remaining cells showed high expression of annexin V (in red) compared to non-treated cells (0 µM dox). In collagen type I gels, embedded SW480

cells formed spheroid-like structures, with dox (1 - 5 μM) causing disruption to spheroid structures and increase in annexin V expression. Finally, SW480 reseeded in CDMs did not form spheroid like-structures, but rather clusters or cell sheets. No increase in annexin V was observed but the morphology of SW480 was altered with increasing dox concentration, causing cell dispersion. SW480 is a metastatic cell line which was previously shown to not form spheroids in 3D cultures but rather having a disperse morphology [90,91]. Our data suggests that the produced CDMs recapitulate more closely the morphology of metastatic cells in complex 3D microenvironment than standard type I collagen gels. This could be related to the complex biochemical composition of CDMs, their porosity and/or stiffness.

These results suggest the importance of the tumor microenvironment, especially the remodeled and stiffer extracellular matrix, in the diffusion and efficacy of antitumoral chemotherapeutic drugs [92,93]. These findings highlight the existing differences between 2D and 3D cultures [92]. In addition, our results indicate that cells grown in cell-produced matrices acquire similar or higher resistance to therapeutics when compared to current standard 3D in vitro culture models. These results further confirm the need for complex 3D matrix models to study drug response and support the use of our development 3D CDMs as an alternative platform for 3D cell culture of cancer cells.

3. Conclusions

In summary, in the present work we have established a 3D hAMSC culturing method using sacrificial PLA MCs and MMCs to obtain large complex three-dimensional CDMs for further use in *in vitro* cancer modeling.

An extensive physical, biochemical and mechanical tissue characterization was carried out to study CDMs properties. Results highlighted the production of mesenchymal soft fibrous tissues at the macroscale, essentially composed of collagen types I, III, IV and fibronectin, main fibrillar

proteins of connective tissues. Moreover, CDM micromechanical measurements suggested that CDMs' stiffness can be tuned by culture conditions, such as agitation. Upon decellularization and MCs removal, resulting CDMs were successfully repopulated using colorectal cancer cell lines, leading to a formation of viable spheroids (cancer cells derived from primary tumor, HT29) or dispersed invasive cancer cell sheets (metastatic cancer cells, SW480). In addition, the doxorubicin cytotoxic drug screening assay revealed CDMs' strong role as a physical barrier against this drug, preventing cell death and showing similar cell-ECM interaction to what has been observed in treated human tumors [42,89,94].

Overall, this novel 3D in vitro CDM platform showed architecture, composition and rigidity features that mimic native stromal microenvironment from human tissues present in the intestines, skin, or organs such as kidney, liver, pancreas and brain. This offers the possibility to generate a plethora of reliable 3D *in vitro* cancer models by tuning the CDM fabrication conditions and by reseeding them with cells of interest. These novel CDMs-based models will be useful in understanding ECM biochemical and biomechanical remodeling processes during disease development. Finally, CDMs models have an enormous potential for screening of therapeutics, in pharmacokinetics and pharmacodynamics studies, and open the possibility to establish the basis for patient-specific testing platforms using patient-derived cells.

4. Materials and methods

4.1. Materials

Poly-lactic acid (70/30 L-lactide/DL-lactide copolymer, PURASORB® PLDL7028) with an inherent viscosity midpoint of 3.8 dL/g and a molecular weight of 850 000 Da, was purchased from Purac, (-)-Ethyl L-lactate (EtLac, photoresist grade; purity >99.0%), Poly(vinyl alcohol) (PVA, 30–70 kDa, 88% hydrolysed), fibronectin, Ficoll® 70 and Ficoll® 400 were purchased

from Sigma Aldrich. Human Adipose Mesenchymal Stem Cells (hAMSCs) were obtained from donors and were kindly provided by Dr. Jeronimo Blanco's research group at Consejo Superior de Investigaciones Científicas (CSIC, Spain).

4.2. Poly-lactic acid microcarriers production and functionalization

Poly-lactic acid (PLA) MCs were produced following a previously published protocol [45,95]. Briefly, PLA was dissolved in EtLac at a concentration of 3.5% (w/v). The polymeric solution was dispensed through the inner bore (30G) of a dual concentric nozzle (NNC-DN-2230, NanoNC, South Korea) at a rate of 10 mL/h. N_2 was fed through the outer bore (22G) at 1bar of pressure. MCs were obtained in a 0.3% PVA in 70% ethanol coagulation bath. The functionalization process consists in a three-step procedure: 10 minutes hydrolysis in a 50 mM NaOH solution; 2 hours activation of the resulting -COOH groups with a ethyl(dimethylaminopropyl) carbodiimide/N-hydroxysuccinimide 100 mM/200 mM (EDC/NHS, Sigma Aldrich) solution in 70% ethanol; and an overnight incubation in 100 µg/ml fibronectin, generating covalent bonds with MCs surface and providing them with a coating for enhanced cell adhesion.

PLA MCs were characterized for size and morphology using SEM images of particles and GraphPad Prism 8 (Prism 8^{TM}, San Diego, CA, United States) to analyze obtained size distribution and statistical parameters.

4.3. Cell culture

4.3.1. Human adipose mesenchymal stem cells (hAMSC)

hAMSC were seeded and expanded in T175 flasks with expansion medium consisting of advanced Dulbecco's modified Eagle's medium (Adv. DMEM; Gibco, #12491023) supplemented with 10% fetal bovine serum (FBS; Sigma Aldrich, #F7524), 100 units/ml Penicillin-Streptomycin

(Pen/Strep; Gibco, #10378016) and 100 µL/mL L-glutamine (L-glut; Gibco, #25020081) at 37ºC and 5% CO2.

4.3.2. Microcarrier (MC) seeding

hAMSCs were trypsinised and seeded on fibronectin-functionalized MC's surface, at a density of 100,000 cells/mg of MC, in a spinner flask for 8 hours as described previously [41]. Cell-seeded MCs were then transferred to ultra-low adhesion 24 well plates (Corning, #3473) in different amounts (Table 1) for 10 or 21-day culture period, adding non-seeded particles at stablished time points. CDMs production was also compared between static and stirred conditions in 10-day cultures [96]. Stirred conditions were achieved by placing plates containing CDMs on a temperature-, high humidity- and CO2- resistant orbital shaker at 35 rpm (Thermo scientific, #88881102) placed inside a cell culture incubator.

Table 1 Microcarriers conditions for CDMs production

Condition	Cell-seeded MCs
A	3 mg/well (no extra addition of MCs)
B	3 mg/well (addition of 1.5mg of MCs at day 3 and 3mg at days 7 and 14)
C	3 mg/well (addition of 3mg of MCs at days 3, 7 and 14)
D	5 mg/well (no extra addition of MCs)
E	10mg/well (no extra addition of MCs)

4.3.3. Macromolecular crowders' (MMCs) density

hAMSCs were seeded in 24 well plates at a density of 20,000 cells/well at 37ºC and 5% CO_2. After 4 hours, cell culture medium was changed to assess the effect of MMCs on extracellular matrix (ECM) deposition [97]. MMCs were prepared by mixing different ratios of Ficoll® 70/400 (Table 2). After 1, 3 and 7 days, cells were processed for total protein deposition and DNA content.

Table 2 FVO and concentrations of Ficoll®

Fraction Volume Occupancy (FVO, % v/v)	Ficoll® 70 kDa (mg/mL)	Ficoll® 400 kDa (mg/mL)
0 % v/v	0 mg/mL	0 mg/mL
9 % v/v	18.75 mg/mL	12.5 mg/mL
14,5 % v/v	25 mg/mL	25 mg/mL
18 % v/v	37.5 mg/mL	25 mg/mL

4.3.4. Cell-derived matrices decellularization and microcarriers removal

Cells were removed from CDMs using 0.5% Triton 100X in 25mM NH_4OH for 30 minutes followed by a second step using a 30 µg/ml solution of DNase I (Sigma Aldrich) in PBS for 1 hour. MCs removal was carried out using 0.5M Na_3PO_4 for 8 hours at 37ºC All steps were performed under sterile conditions.

4.3.5. Colorectal cancer cell lines

Decellularized and MC-free CDMs were washed in PBS and placed in 96-well ultra-low attachment plates (Corning, #3474). To reseed CDMs with HT29 or SW480 colorectal cancer cell lines, 10^5 cells/sample were seeded on top of the CDMs in a total volume of 20 µL of supplemented Adv. DMEM medium containing MMCs. Following 1-hour incubation, 200 µL of medium were added on top of the CDMs.

4.3.6. Doxorubicin screening

Reseeded CDMs were cultured for 7 days, with daily medium change, before Doxorubicin (Dox) cytotoxicity evaluation. As control we used collagen type I gels (OptiCol™ Human Collagen Type I; Cell guidance systems, #M16S) containing 10^5 cells/gel and 2D cultures (10^4 cells/well in 96-well-plates). Samples were incubated in different concentrations of Dox chemotherapeutic drug (0, 0.5, 1 and 5µM) for a total 120-hour period. Cell viability was quantified using alamarBlue™

(Invitrogen, #DAL1025) at 24, 72 and 120-hour time points. Briefly, reseeded CDMs, collagen gels and 2D cells were incubated for 4 hours in a 1:9 dilution of alamarBlue™ in cell culture medium. Afterwards, the supernatant was collected, and absorbance was measured at 570nm.

4.4. DNA quantification

PicoGreen assay was performed to measure the amount of double stranded DNA (dsDNA) in CDMs following the manufacturer's protocol. Briefly, CDMs were washed with PBS and incubated in 1X Tris-EDTA (TE) buffer for 30 minutes at 4ºC. Samples were frozen and thawed three times and then mechanically disrupted with a tissue homogenizer (Kinematica AG, #PT 1200 E). A sonication step was performed to help in dsDNA extraction. Samples were centrifuged at 1500 rpm for 10 minutes at 4ºC and dsDNA in supernatant was measured by fluorescence at an excitation/emission wavelength of 480/520 nm using Quant-iT™ PicoGreen® kit (Thermo Fisher). A calibration curve was performed for DNA concentration calculations. Three samples were measured per condition with three replicates per sample (N=3, n=3).

4.5. Total protein quantification

Bicinchoninic acid (BCA) assay was performed for colorimetric quantitation of total protein. Briefly, CDMs were washed with PBS and incubated in M-PER lysis buffer for 30 minutes at 4ºC. Samples were frozen and thawed three times followed by mechanical disruption with a tissue homogenizer (Kinematica AG). A sonication step was performed to help in protein disruption and solubilization. Samples were centrifuged at 14,000 g for 15 minutes at 4ºC discarding the obtained pellet of cell debris and PLA MCs. The absorbance of the supernatant was measured at 562 nm using Pierce BCA Protein Assay kit (Thermo Fisher). A calibration curve was performed for protein concentration calculations. Three samples were measured per condition with three replicates per sample (N=3, n=3).

4.6. Surface topography analysis

CDMs morphology and physical properties were observed using Scanning Electron Microscope (SEM, NOVA NanoSEM 230, FEI Company). Samples were fixed for 30 minutes in 4% paraformaldehyde (PFA) at room temperature and dried sequentially in ethanol baths (20, 40, 60, 80, 96 and 100%). Then samples underwent a supercritical drying process followed by a carbon coating and were analyzed at 5 kV. Three samples were measured per condition with three replicates per sample (N=3, n=3).

4.7. Gene expression quantification

Gene expression of ECM fibrillar proteins (fibronectin and collagens type I, III, and IV) was quantified using real-time reverse transcriptase polymerase chain reaction (qRT-PCR). CDMs were washed with PBS and stored at -20ºC in RTL buffer. Qiagen RNeasy® Plus Mini Kit (Qiagen, #74134) was used to purify RNA from samples. RNA purity and concentration were quantified using NanoDrop Spectrophotometer (ND-1000, NanoDrop®), followed by RNA conversion into cDNA using RT2 First Strand Kit (Qiagen, #330404). cDNA was mixed with RT2 SYBR Green ROX qPCR Mastermix (Qiagen, #330524) and primers mix. The following primers were used: Human Beta Actin (ACTB; Qiagen, PPH00073G-200) as the house keeping gene, collagen type I (COL1A1; Qiagen, 524PPH01299F-200); collagen type III (COL3A1; Qiagen, 524PPH00439F-200); collagen type IV (COL4A1; Qiagen, 524PPH20687A-200); and Fibronectin (FN) forward 5'-CCAGGCAGTACAATGTGGGT-3', reverse 5'-TGGAATAGAGCTCCCAGGCT-3'. Primers' efficiency was tested and validated for further experiments and RNA purity was also assessed and validated for every analyzed sample. Human RNA (Human XpressRef Universal Total RNA, Qiagen, #338112) was used as a positive and interplate control to compensate variations between plates. Real-time PCR (Real Time PCR system

Step One Plus; Applied biosystems) was carried out under the following conditions: 10 minutes at 95ºC followed by 40 cycles of 15s at 95ºC and 1 minute at 60ºC. Finally, a melting curve was performed having plates 15s at 95ºC, followed by 1 minute at 60ºC and the melting step from 60 to 95ºC. Relative gene-fold variations were determined by the $2^{-\Delta\Delta Ct}$ method using Beta Actin as the housekeeping gene and compared to a control sample consisting of 2D cultured hAMSCs in absence of MMCs. Three samples were measured per condition with three replicates per sample (N=3, n=3).

4.8. Immunofluorescent staining

For immunofluorescence staining of ECM proteins and MCs' surface coating, cell-containing CDMs were washed in PBS, fixed in 4% PFA for 30 minutes at 4ºC and stored in PBS with 0.15% w/v glycine and 0.2% w/v sodium azide until needed. 0.25% v/v Triton 100X in PBS and 0.15% w/v glycine was used for cell permeabilization for 10 minutes. Blocking step was performed in PBS with 0.15% w/v glycine and 3% w/v bovine serum albumin (BSA) for 30 min (cell-free CDMs and MCs' staining processes start at this step). Primary antibodies were incubated overnight in PBS, 0.15% w/v glycine and 3% w/v BSA at 4ºC (Table 3). Secondary antibodies were incubated for 1 hour at room temperature in PBS with 0.15% w/v glycine and 3% w/v BSA (Table 3). Cell-containing CDM samples were incubated with 1µg/ml DAPI solution in PBS, 0.15% w/v glycine and 3% BSA for 1 minute at room temperature. Finally, samples were washed in PBS with 0.15% glycine, mounted in Ibidi® µ-Dish 35mm dishes (Ibidi®; #81151) and imaged using a Zeiss LSM 780 confocal microscope (Germany) equipped with a 25x (NA=0.85) multi-immersion and a 40x (NA=1.2) water immersion lenses. Three samples were imaged per condition (n=3) and multichannel 3D reconstruction was performed using a voxel size of 1x1x1 pixels. MCs were washed in PBS with 0.15% glycine after secondary antibody incubation, mounted and covered in

Superfrost® Plus slides (Thermo Scientific, J1800AMNZ) with No. 1.5 coverslips (Duran group, #2355035) and imaged under Nikon Eclipse E600 epifluorescence microscope (Japan). Random sampling was stained and analyzed from three different MC batches (n=3).

4.9. CDM histology and immunofluorescent staining

Histological sections of cell-containing and cell-free CDMs were stained for ECM proteins identification and quantification. Firstly, CDMs were rinsed in sequential 10, 20 and 30% w/v sucrose baths, embedded in optimal cutting temperature compound (OCT, #4583; Tissue-Tek®) and frozen at -20ºC. Histological cuts were done at 50 µm thickness using Leica CM 1900 cryostat (Germany) at -24ºC, collected in Superfrost® Plus slides (Thermo Scientific; J1800AMNZ) and stored at -20ºC. For immunofluorescence staining, histology slides were thawed, OCT was washed with milliQ water and staining was carried out as described in previous section (2.8, Table 3). Following staining, samples were mounted with Fluoromount-G® mounting media (Southern Biotech, #0100-01) and imaged using a Thunder 3D Live Cell microscope (Leica Microsystems) equipped with a 20x (NA=0.75) multi-immersion and a 63x (NA=1.2) water immersion objectives. Three samples were stained per condition (n=3) and multichannel 3D reconstruction was performed. For the quantification of the tissues: sampling of 15 fields per tissue (n = 3) were performed using a voxel size of 0.1x0.1x0.26 µm and a total thickness of 3 µm. On line classical deconvolution (Lucy Richardson algorithm) was run in parallel to remove out of focus light.

Table 3 Antibodies and dyes used for immunofluorescent staining.

Assay	Primary antibodies	Secondary antibodies	Additional dye/s
Cell-containing samples			
CDM qualitative staining	Anti-Collagen I antibody (Mouse; ab6308); dil. 1:500	Donkey Anti-Mouse IgG H&L (CF™ 594; SAB4600098); dil. 1:500	DAPI (D9542); 1µg/ml

	Anti-Collagen III antibody (Rabbit; ab7778); dil. 1:500	Goat Anti-Rabbit IgG H&L (Alexa Fluor® 488; ab150077); dil. 1:500	
Cell-free samples			
MCs' surface staining	Anti-Fibronectin antibody (Mouse; ab6328); dil. 1:500	Goat Anti-Mouse IgG H&L (Alexa Fluor® 488; ab150117); dil. 1:500	
Quantitative CDM staining	Anti-Collagen I antibody (Mouse; ab6308); dil. 1:500	Donkey Anti-Mouse IgG H&L (Alexa Fluor® 647; ab150107); dil. 1:500	
	Anti-Collagen IV antibody (Rabbit; ab6586); dil. 1:500	Donkey Anti-Rabbit IgG H&L (Alexa Fluor® 568; ab175470); dil. 1:500	
	Anti-Fibronectin antibody (Mouse; ab6328); dil. 1:500	Goat Anti-Mouse IgG H&L (Alexa Fluor® 488; ab150117); dil. 1:500	
	Anti-Collagen III antibody (Rabbit; ab7778); dil. 1:500	Donkey Anti-Rabbit IgG H&L (Alexa Fluor® 488; ab150077); dil. 1:500	
Doxorubicin cytotoxicity assay	Anti-Collagen I antibody (Mouse; ab6308); dil. 1:500	Donkey Anti-Mouse IgG H&L (Alexa Fluor® 647; ab150107); dil. 1:500	DAPI (D9542); 1µg/ml
	Anti-Annexin V antibody (Rabbit; ab14196); dil. 1:200	Donkey Anti-Rabbit IgG H&L (Alexa Fluor® 568; ab175470); dil. 1:500	Acti-stain 488 phalloidin (PHDG1-A); dil. 1:200

4.10. Live/dead staining

Live/dead staining was performed to cell-seeded MCs and 10-day cultured CDMs to evaluate cell viability. Briefly, samples were washed three times in 1x DPBS (Gibco; #14190144) for five minutes. A 20 minutes viable cell staining was performed using 2µM Calcein AM (green labelling; Abcam; #275925) and a 4µM Propidium iodide (Sigma Aldrich; #25535-16-4) solution in DPBS at 37 ºC. Cell-seeded MCs were washed once in DPBS for five minutes, mounted on microscope slides and rapidly imaged under a Nikon Eclipse E600 epifluorescence microscope (Japan). CDMs were washed once in DPBS for five minutes, cut longitudinally using scalpels and mounted in Ibidi® µ-Dish 35mm dishes (Ibidi®; #81151) and imaged under a Thunder 3D Live Cell microscope (Leica Microsystems).

4.11. Protein quantification by fluorescence staining

4.11.1. DOT blot fluorescence calibration

In order to calibrate and correlate the fluorescent intensity obtained for each of the proteins analyzed (Table 3, two-step quantitative CDM staining) to concentration values, DOT blot technique was used. Briefly, nitrocellulose membranes were cut in 10x20mm square shape and placed on microscope slides. 0.5 µl drops of each protein (N=9) were placed on top of the membranes and pH crosslinked with saline solution for 1h at room temperature (Table 4). Immunofluorescence staining was performed as in section 2.8 starting from blocking step. Negative controls of primary antibodies were performed for all proteins analyzed. After staining, membranes were mounted with Fluoromount-G®, covered with No. 1.5 coverslips and imaged using the Thunder 3D Live Cell microscope, set at the exact same parameters used to image CDM samples. Each protein drop was completely imaged as a mosaic, using the exact voxel size and number of Zs, and same on line deconvolution parameters were applied (Fig. S5).

Table 4 Protein controls for fluorescence intensity calibration

Protein	Concentration
OptiCol™ Human Collagen Type I (Cell guidance systems, #M16S)	3.8mg/ml
OptiCol™ Human Collagen Type III (Cell guidance systems, #M20S)	0.75mg/ml
Collagen from human placenta; Bornstein and Traub Type IV (Sigma, #C7521)	1mg/ml
Fibronectin human plasma (Sigma, #F0895)	0.2mg/ml

4.11.2. Fluorescence quantification

To quantify the protein content in CDMs using fluorescent images, we used the Dot blot protein images for calibration (Fig. S5). Using FIJI ImageJ software, we generated a fluorescence quantification macro for the calibration images and a second macro to quantify fluorescence

intensity of the three collagen types studied and fibronectin (protein calibration and calibration rationales can be found at Fig. S6). Once fluorescence intensities from calibration and samples images were obtained, the final protein amounts (in µg) were calculated with the known calibration protein concentrations. Detailed protocol and macros information can be found in the supporting information.

4.12. Mass spectrometry for CDM composition analysis

Qualitative characterization of CDMs composition was performed using mass spectrometry. Briefly, decellularized and MCs' free CDMs were freeze-dried. Samples were digested, cleaned-up, dried-down and stored at -20ºC. The dried-down peptide mixtures were analyzed using nanoAcquity liquid chromatographer (Waters) coupled to an LTQ-Orbitrap Velos (Thermo Scientific) mass spectrometer. Eluted peptides were subjected to electrospray ionization in an emitter needle (PicoTipTM, New Objective). Peptide masses were analyzed in data dependent mode where a full Scan Mass Spectrometry (MS) was acquired. The .raw files obtained in the mass spectrometry analysis were used to search against the public database SwissProt human (see supporting information).

4.13. Assessment of CDM micromechanical properties using Atomic Force Microscopy

Decellularized and MCs-free CDMs were embedded in OCT and frozen at -80ºC. 12 µm histological slices were obtained by cryosectioning (CM3050S, Leica Biosystems, Germany) and placed on top of positively charged glass slides. For sample analysis under atomic force microscope (AFM), OCT was removed by washing samples three times with PBS.

Micromechanical properties of the sample were measured in PBS buffer at 37 ºC pH 7.4 using a custom-built AFM mounted on an inverted optical microscope (TE2000, Nikon, Tokio, Japan).

Measurements were performed by doing force-displacement curves on the surface of the sample with V-shaped silicon nitride cantilevers (0.01 N/m of nominal spring constant) ended with a 2.25 μm radius spherical polystyrene bead (Novascan Technologies, Ames, IA). The vertical position of the cantilever was controlled by a piezoelectric actuator and measured with strain gauge sensors (Physik Instrumente, Karlsruhe, Germany), and a four-quadrant photodiode (S4349, Hamamatsu, Japan) was employed to measure cantilever deflection. Elastic modulus was computed from the force-displacement curves by adjusting the Hertz model as described in [98] by using a custom software implemented in MATLAB (MathWorks, Natick, MA). Micromechanics of CDMs were probed in 5 randomly selected zones of the sample. Twenty-five force curves (10 μm amplitude at a speed of 5 μm/s) were recorded for each zone in five different points (five curves/probing point) randomly selected and separated at least 10 μm form each other in the XY dimensions.

4.14. Statistical analysis

Obtained results are expressed as mean ± SD. Statistical differences were assessed using GraphPad Prism 8. Normality test (Gaussian distribution) was performed to assess data normal distribution. After normality test, one-way (parametric or nonparametric) or two-way ANOVA tests, followed by Tukey post analysis, unless stated. Statistical significance was considered at a value of $\alpha<0.05$, and represented as follows: *$p<0.05$, **$p<0.01$, ***$p<0.001$, ****$p<0.0001$.

ASSOCIATED CONTENT

Supporting Information

- **Supporting figures**

Total DNA and protein quantification results from Macromolecular Crowders' cell culture optimization (Figure S1); PLA microcarriers characterization (Figure S2); CDM morphology and final size (Figure S3); CDM cell viability assessment (Figure S4); CDMs' physical characterization using SEM (Figure S5); CDM repopulation using HT29/SW480 colorectal cancer cell lines (Figure S6).

- **Supporting methods**

Protein DOT blots fluorescence calibration (Figure S7); Protein quantification through immunofluorescence staining (Figure S8); Antibody specificity controls (Figure S9); Mass spectrometry supporting methodology.

- **Supporting results**

qRT-PCR primer efficiencies; Nanodrop RNA concentration and purity results.

AUTHOR INFORMATION

Corresponding Author

Elisabeth Engel - Institute for Bioengineering of Catalonia (IBEC), The Barcelona Institute of Science and Technology, Barcelona, Spain; Email: eengel@ibecbarcelona.eu

Miguel A. Mateos-Timoneda - Institute for Bioengineering of Catalonia (IBEC), The Barcelona Institute of Science and Technology, Barcelona, Spain; Email: mamateos@ibecbarcelona.eu

Present Addresses

Agata Nyga – MRC Laboratory of Molecular Biology, Cambridge – United Kingdom

Miguel A. Mateos Timoneda - Bioengineering Institute of Technology, Universitat Internacional de Catalunya (UIC), Sant Cugat del Vallès (Barcelona), Spain

Author Contributions

G.R.S. carried out all experiments with help from A.N., E.R. and J.O. The manuscript was written by G.R.S. with corrections of all authors. All authors have given approval to the final version of the manuscript.

Funding Sources

Researchers thank MICIU (BES-2016-077182, MAT2015-68906-R, RTI2018-096320-B-C21, PGC2018-097323-A-I00, DPI2017-83721-P) and the Spanish network of cell therapy (TERCEL) for financial support. Finally, researchers also thank Programme/Generalitat de Catalunya (2017-SGR-359) and the Severo Ochoa programme of the Spanish Ministry of Science and Competitiveness (Grant SEV-2014-0425, 2015-2019).

Notes

Authors declare no competing financial interest. Supporting data for the present study is available from authors upon reasonable request.

ACKNOWLEDGMENTS

Researchers would like to thank Prof. Alberto Muñoz Terol group (IIB-UAM) for the donation of colorectal cancer cell lines. The proteomics platform from Barcelona scientific park (PCB) is acknowledged for their help in acquisition and analysis of mass spectrometry results. Judit Linacero from MicroFabSpace is acknowledged for help and training in SEM microscopy. Molecular Imaging Platform at Molecular Biology Institute of Barcelona (MIP IBMB-PCB) is also acknowledged for training and imaging of samples. We also acknowledge Leica Microsystems for support to the MIP IBMB-PCB on the Thunder collaborative project.

REFERENCES

(1) Hynes, R. O. Extracellular Matrix: Not Just Prety Fibrils. *Science (80-.).* **2009**, *326* (5957), 1216–1219. https://doi.org/10.1126/science.1176009.Extracellular.

(2) Bonnans, C.; Chou, J.; Werb, Z. Remodelling the Extracellular Matrix in Development and Disease. *Nature Reviews Molecular Cell Biology*. Nature Publishing Group December 11, 2014, pp 786–801. https://doi.org/10.1038/nrm3904.

(3) Frantz, C.; Stewart, K. M.; Weaver, V. M. The Extracellular Matrix at a Glance. *J. Cell Sci.* **2010**, *123* (24), 4195–4200. https://doi.org/10.1242/jcs.023820.

(4) Hynes, R. O.; Naba, A. Overview of the Matrisome-An Inventory of Extracellular Matrix Constituents and Functions. *Cold Spring Harb. Perspect. Biol.* **2012**, *4* (1). https://doi.org/10.1101/cshperspect.a004903.

(5) Guilak, F.; Cohen, D. M.; Estes, B. T.; Gimble, J. M.; Liedtke, W.; Chen, C. S. Control of Stem Cell Fate by Physical Interactions with the Extracellular Matrix. *Cell Stem Cell*. July 2, 2009, pp 17–26. https://doi.org/10.1016/j.stem.2009.06.016.

(6) Kim, S. H.; Turnbull, J.; Guimond, S. Extracellular Matrix and Cell Signalling: The Dynamic Cooperation of Integrin, Proteoglycan and Growth Factor Receptor. *Journal of Endocrinology*. May 2011, pp 139–151. https://doi.org/10.1530/JOE-10-0377.

(7) Geiger, B.; Bershadsky, A.; Pankov, R.; Yamada, K. M. Transmembrane Extracellular Matrix-Cytoskeleton Crosstalk. *Nat. Rev. Mol. Cell Biol.* **2001**, *2* (11), 793–805. https://doi.org/10.1038/35099066.

(8) Discher, D. E.; Mooney, D. J.; Zandstra, P. W. Growth Factors, Matrices, and Forces Combine and Control Stem Cells. *Science*. June 26, 2009, pp 1673–1677. https://doi.org/10.1126/science.1171643.

(9) Lukashev, M. E.; Werb, Z. ECM Signalling: Orchestrating Cell Behaviour and

Misbehaviour. *Trends Cell Biol.* **1998**, *8* (11), 437–441. https://doi.org/10.1016/S0962-8924(98)01362-2.

(10) Iozzo, R. V.; Gubbiotti, M. A. Extracellular Matrix: The Driving Force of Mammalian Diseases. *Matrix Biology*. Elsevier B.V. October 1, 2018, pp 1–9. https://doi.org/10.1016/j.matbio.2018.03.023.

(11) Sainio, A.; Järveläinen, H. Extracellular Matrix-Cell Interactions: Focus on Therapeutic Applications. *Cell. Signal.* **2020**, *66*, 109487. https://doi.org/10.1016/j.cellsig.2019.109487.

(12) Boudreau, N.; Bissell, M. J. Extracellular Matrix Signaling: Integration of Form and Function in Normal and Malignant Cells. *Curr. Opin. Cell Biol.* **1998**, *10* (5), 640–646. https://doi.org/10.1016/S0955-0674(98)80040-9.

(13) Hastings, J. F.; Skhinas, J. N.; Fey, D.; Croucher, D. R.; Cox, T. R. The Extracellular Matrix as a Key Regulator of Intracellular Signalling Networks. *Br. J. Pharmacol.* **2019**, *176* (1), 82–92. https://doi.org/10.1111/bph.14195.

(14) Cukierman, E.; Pankov, R.; Stevens, D. R.; Yamada, K. M. Taking Cell-Matrix Adhesions to the Third Dimension. *Science (80-.).* **2001**, *294* (5547), 1708–1712. https://doi.org/10.1126/science.1064829.

(15) Fitzpatrick, L. E.; McDevitt, T. C. Cell-Derived Matrices for Tissue Engineering and Regenerative Medicine Applications. *Biomater. Sci.* **2015**, *3* (1), 12–24. https://doi.org/10.1039/C4BM00246F.

(16) Prewitz, M. C.; Seib, F. P.; Von Bonin, M.; Friedrichs, J.; Stißel, A.; Niehage, C.; Müller, K.; Anastassiadis, K.; Waskow, C.; Hoflack, B.; Bornhäuser, M.; Werner, C. Tightly Anchored Tissue-Mimetic Matrices as Instructive Stem Cell Microenvironments. *Nat. Methods* **2013**, *10* (8), 788–794. https://doi.org/10.1038/nmeth.2523.

(17) Matsuura, K.; Utoh, R.; Nagase, K.; Okano, T. Cell Sheet Approach for Tissue Engineering and Regenerative Medicine. *J. Control. Release* **2014**, *190*, 228–239. https://doi.org/https://doi.org/10.1016/j.jconrel.2014.05.024.

(18) Liao, J.; Guo, X.; Grande-Allen, K. J.; Kasper, F. K.; Mikos, A. G. Bioactive Polymer/Extracellular Matrix Scaffolds Fabricated with a Flow Perfusion Bioreactor for Cartilage Tissue Engineering. *Biomaterials* **2010**, *31* (34), 8911–8920. https://doi.org/https://doi.org/10.1016/j.biomaterials.2010.07.110.

(19) Zhou, X.; Yang, A.; Huang, Z.; Yin, G.; Pu, X.; Jin, J. Enhancement of Neurite Adhesion, Alignment and Elongation on Conductive Polypyrrole-Poly(Lactide Acid) Fibers with Cell-Derived Extracellular Matrix. *Colloids Surfaces B Biointerfaces* **2017**, *149*, 217–225. https://doi.org/https://doi.org/10.1016/j.colsurfb.2016.10.014.

(20) Navone, S. E.; Pascucci, L.; Dossena, M.; Ferri, A.; Invernici, G.; Acerbi, F.; Cristini, S.; Bedini, G.; Tosetti, V.; Ceserani, V.; Bonomi, A.; Pessina, A.; Freddi, G.; Alessandrino, A.; Ceccarelli, P.; Campanella, R.; Marfia, G.; Alessandri, G.; Parati, E. A. Decellularized Silk Fibroin Scaffold Primed with Adipose Mesenchymal Stromal Cells Improves Wound Healing in Diabetic Mice. *Stem Cell Res. Ther.* **2014**, *5* (1), 7. https://doi.org/10.1186/scrt396.

(21) Harvestine, J. N.; Saiz Augustine M., J.; Leach, J. K. Cell-Secreted Extracellular Matrix Influences Cellular Composition Sequestered from Unprocessed Bone Marrow Aspirate for Osteogenic Grafts. *Biomater. Sci.* **2019**, *7* (5), 2091–2101. https://doi.org/10.1039/C8BM01478G.

(22) Yuan, M.; Pai, P. J.; Liu, X.; Lam, H.; Chan, B. P. Proteomic Analysis of Nucleus Pulposus Cell-Derived Extracellular Matrix Niche and Its Effect on Phenotypic Alteration of Dermal Fibroblasts. *Sci. Rep.* **2018**, *8* (1), 1–15. https://doi.org/10.1038/s41598-018-19931-9.

(23) Cheng, H.-W.; Tsui, Y.-K.; Cheung, K. M. C.; Chan, D.; Chan, B. P. Decellularization of Chondrocyte-Encapsulated Collagen Microspheres: A Three-Dimensional Model to Study the Effects of Acellular Matrix on Stem Cell Fate. *Tissue Eng. Part C Methods* **2009**, *15* (4), 697–706. https://doi.org/10.1089/ten.tec.2008.0635.

(24) Pati, F.; Song, T.-H.; Rijal, G.; Jang, J.; Kim, S. W.; Cho, D.-W. Ornamenting 3D Printed Scaffolds with Cell-Laid Extracellular Matrix for Bone Tissue Regeneration. *Biomaterials* **2015**, *37*, 230–241. https://doi.org/https://doi.org/10.1016/j.biomaterials.2014.10.012.

(25) Lee, H. J.; Kim, Y. B.; Ahn, S. H.; Lee, J.-S.; Jang, C. H.; Yoon, H.; Chun, W.; Kim, G. H. A New Approach for Fabricating Collagen/ECM-Based Bioinks Using Preosteoblasts and Human Adipose Stem Cells. *Adv. Healthc. Mater.* **2015**, *4* (9), 1359–1368. https://doi.org/10.1002/adhm.201500193.

(26) Lu, H.; Hoshiba, T.; Kawazoe, N.; Koda, I.; Song, M.; Chen, G. Cultured Cell-Derived Extracellular Matrix Scaffolds for Tissue Engineering. *Biomaterials* **2011**, *32* (36), 9658–9666. https://doi.org/10.1016/j.biomaterials.2011.08.091.

(27) Lu, H.; Hoshiba, T.; Kawazoe, N.; Chen, G. Autologous Extracellular Matrix Scaffolds for Tissue Engineering. *Biomaterials* **2011**, *32*, 2489–2499. https://doi.org/10.1016/j.biomaterials.2010.12.016.

(28) Franco-Barraza, J.; Beacham, D. A.; Amatangelo, M. D.; Cukierman, E. Preparation of Extracellular Matrices Produced by Cultured and Primary Fibroblasts. *Curr Protoc Cell Biol.* **2017**, *71* (3), 10.9.1–10.9.34. https://doi.org/10.1002/cpcb.2.

(29) Yamada, K. M.; Cukierman, E. Modeling Tissue Morphogenesis and Cancer in 3D. *Cell* **2007**, *130* (4), 601–610. https://doi.org/10.1016/j.cell.2007.08.006.

(30) Rubi-Sans, G.; Castaño, O.; Cano, I.; Mateos-Timoneda, M. A.; Perez-Amodio, S.; Engel, E. Engineering Cell-Derived Matrices: From 3D Models to Advanced Personalized Therapies. *Advanced Functional Materials*. 2020, p 2000496. https://doi.org/10.1002/adfm.202000496.

(31) Pavez Loriè, E.; Boukamp, P. Methods in Cell Biology: Cell-Derived Matrices. *Methods Cell Biol.* **2020**, *156*, 309–332. https://doi.org/10.1016/BS.MCB.2019.11.012.

(32) M, B.; S, P.-W.; JR, B.; P, B. Three-Dimensional In Vitro Skin and Skin Cancer Models Based on Human Fibroblast-Derived Matrix. *Tissue Eng. Part C. Methods* **2015**, *21* (9), 958–970. https://doi.org/10.1089/TEN.TEC.2014.0698.

(33) Bell, E.; Ehrlich, H.; Buttle, D.; Nakatsuji, T. Living Tissue Formed in Vitro and Accepted as Skin-Equivalent Tissue of Full Thickness. *Science* **1981**, *211* (4486), 1052–1054.

https://doi.org/10.1126/SCIENCE.7008197.

(34) Stark, H. J.; Boehnke, K.; Mirancea, N.; Willhauck, M. J.; Pavesio, A.; Fusenig, N. E.; Boukamp, P. Epidermal Homeostasis in Long-Term Scaffold-Enforced Skin Equivalents. *J. Investig. Dermatology Symp. Proc.* **2006**, *11* (1), 93–105. https://doi.org/10.1038/SJ.JIDSYMP.5650015.

(35) Stark, H. J.; Willhauck, M. J.; Mirancea, N.; Boehnke, K.; Nord, I.; Breitkreutz, D.; Pavesio, A.; Boukamp, P.; Fusenig, N. E. Authentic Fibroblast Matrix in Dermal Equivalents Normalises Epidermal Histogenesis and Dermo-Epidermal Junction in Organotypic Co-Culture. *Eur. J. Cell Biol.* **2004**, *83* (11–12), 631–645. https://doi.org/10.1078/0171-9335-00435.

(36) Boehnke, K.; Mirancea, N.; Pavesio, A.; Fusenig, N. E.; Boukamp, P.; Stark, H. J. Effects of Fibroblasts and Microenvironment on Epidermal Regeneration and Tissue Function in Long-Term Skin Equivalents. *Eur. J. Cell Biol.* **2007**, *86* (11–12), 731–746. https://doi.org/10.1016/J.EJCB.2006.12.005.

(37) El Ghalbzouri, A.; Siamari, R.; Willemze, R.; Ponec, M. Leiden Reconstructed Human Epidermal Model as a Tool for the Evaluation of the Skin Corrosion and Irritation Potential According to the ECVAM Guidelines. *Toxicol. Vitr.* **2008**, *22* (5), 1311–1320. https://doi.org/10.1016/J.TIV.2008.03.012.

(38) El Ghalbzouri, A.; Commandeur, S.; Rietveld, M. H.; Mulder, A. A.; Willemze, R. Replacement of Animal-Derived Collagen Matrix by Human Fibroblast-Derived Dermal Matrix for Human Skin Equivalent Products. *Biomaterials* **2009**, *30* (1), 71–78. https://doi.org/10.1016/J.BIOMATERIALS.2008.09.002.

(39) Chiang, C.-E.; Fang, Y.-Q.; Ho, C.-T.; Assunção, M.; Lin, S.-J.; Wang, Y.-C.; Blocki, A.; Huang, C.-C. Bioactive Decellularized Extracellular Matrix Derived from 3D Stem Cell Spheroids under Macromolecular Crowding Serves as a Scaffold for Tissue Engineering. *Adv. Healthc. Mater.* **2021**, *10* (11), 2100024. https://doi.org/10.1002/ADHM.202100024.

(40) Xiao, B.; Rao, F.; Guo, Z. Y.; Sun, X.; Wang, Y. G.; Liu, S. Y.; Wang, A. Y.; Guo, Q. Y.; Meng, H. Y.; Zhao, Q.; Peng, J.; Wang, Y.; Lu, S. B. Extracellular Matrix from Human Umbilical Cordderived Mesenchymal Stem Cells as a Scaffold for Peripheral Nerve Regeneration. *Neural Regen. Res.* **2016**, *11* (7), 1172–1179. https://doi.org/10.4103/1673-5374.187061.

(41) Rubí-Sans, G.; Cano-Torres, I.; Pérez-Amodio, S.; Blanco-Fernandez, B.; Mateos-Timoneda, M. A.; Engel, E. Development and Angiogenic Potential of Cell-Derived Microtissues Using Microcarrier-Template. *Biomedicines* **2021**, *9* (3), 232. https://doi.org/10.3390/BIOMEDICINES9030232.

(42) Henke, E.; Nandigama, R.; Ergün, S. Extracellular Matrix in the Tumor Microenvironment and Its Impact on Cancer Therapy. *Frontiers in Molecular Biosciences*. Frontiers Media S.A. January 31, 2020, p 160. https://doi.org/10.3389/fmolb.2019.00160.

(43) Conti, J. A.; Kendall, T. J.; Bateman, A.; Armstrong, T. A.; Papa-Adams, A.; Xu, Q.; Packham, G.; Primrose, J. N.; Benyon, R. C.; Iredale, J. P. The Desmoplastic Reaction Surrounding Hepatic Colorectal Adenocarcinoma Metastases Aids Tumor Growth and

Survival via Av Integrin Ligation. *Clin. Cancer Res.* **2008**, *14* (20), 6405–6413. https://doi.org/10.1158/1078-0432.CCR-08-0816.

(44) Kumar, P.; Satyam, A.; Fan, X.; Collin, E.; Rochev, Y.; Rodriguez, B. J.; Gorelov, A.; Dillon, S.; Joshi, L.; Raghunath, M.; Pandit, A.; Zeugolis, D. I. Macromolecularly Crowded in Vitro Microenvironments Accelerate the Production of Extracellular Matrix-Rich Supramolecular Assemblies. *Sci. Rep.* **2015**, *5*, 1–10. https://doi.org/10.1038/srep08729.

(45) Levato, R.; Mateos-Timoneda, M. A.; Planell, J. A. Preparation of Biodegradable Polylactide Microparticles via a Biocompatible Procedure. *Macromol. Biosci.* **2012**, *12* (4), 557–566. https://doi.org/10.1002/mabi.201100383.

(46) Parisi, L.; Toffoli, A.; Ghezzi, B.; Mozzoni, B.; Lumetti, S.; Macaluso, G. M. A Glance on the Role of Fibronectin in Controlling Cell Response at Biomaterial Interface. *Jpn. Dent. Sci. Rev.* **2020**, *56* (1), 50. https://doi.org/10.1016/J.JDSR.2019.11.002.

(47) Yi, W.; Xiao, E.; Ding, R.; Luo, P.; Yang, Y. High Expression of Fibronectin Is Associated with Poor Prognosis, Cell Proliferation and Malignancy via the NF-KB/P53-Apoptosis Signaling Pathway in Colorectal Cancer. *Oncol. Rep.* **2016**, *36* (6), 3145. https://doi.org/10.3892/OR.2016.5177.

(48) McMurtrey, R. J. Analytic Models of Oxygen and Nutrient Diffusion, Metabolism Dynamics, and Architecture Optimization in Three-Dimensional Tissue Constructs with Applications and Insights in Cerebral Organoids. *Tissue Eng. - Part C Methods* **2016**, *22* (3), 221–249. https://doi.org/10.1089/ten.tec.2015.0375.

(49) Wu, J.; Rostami, M. R.; Cadavid Olaya, D. P.; Tzanakakis, E. S. Oxygen Transport and Stem Cell Aggregation in Stirred-Suspension Bioreactor Cultures. *PLoS One* **2014**, *9* (7), e102486. https://doi.org/10.1371/journal.pone.0102486.

(50) Harris, G. M.; Raitman, I.; Schwarzbauer, J. E. Cell-Derived Decellularized Extracellular Matrices. *Methods Cell Biol.* **2018**, *143*, 97–114. https://doi.org/10.1016/bs.mcb.2017.08.007.

(51) Wang, W.; Itaka, K.; Ohba, S.; Nishiyama, N.; Chung, U. il; Yamasaki, Y.; Kataoka, K. 3D Spheroid Culture System on Micropatterned Substrates for Improved Differentiation Efficiency of Multipotent Mesenchymal Stem Cells. *Biomaterials* **2009**, *30* (14), 2705–2715. https://doi.org/10.1016/j.biomaterials.2009.01.030.

(52) Sakaguchi, K.; Shimizu, T.; Okano, T. Construction of Three-Dimensional Vascularized Cardiac Tissue with Cell Sheet Engineering. *J. Control. Release* **2015**, *205*, 83–88. https://doi.org/10.1016/j.jconrel.2014.12.016.

(53) Frantz, C.; Stewart, K. M.; Weaver, V. M. The Extracellular Matrix at a Glance. *Journal of Cell Science*. December 15, 2010, pp 4195–4200. https://doi.org/10.1242/jcs.023820.

(54) Pöschl, E.; Schlötzer-Schrehardt, U.; Brachvogel, B.; Saito, K.; Ninomiya, Y.; Mayer, U. Collagen IV Is Essential for Basement Membrane Stability but Dispensable for Initiation of Its Assembly during Early Development. *Development* **2004**, *131* (7), 1619–1628. https://doi.org/10.1242/dev.01037.

(55) Nillesen, S. T. M.; Geutjes, P. J.; Wismans, R.; Schalkwijk, J.; Daamen, W. F.; van

Kuppevelt, T. H. Increased Angiogenesis and Blood Vessel Maturation in Acellular Collagen–Heparin Scaffolds Containing Both FGF2 and VEGF. *Biomaterials* **2007**, *28* (6), 1123–1131. https://doi.org/10.1016/J.BIOMATERIALS.2006.10.029.

(56) Zhao, F.; Grayson, W. L.; Ma, T.; Irsigler, A. Perfusion Affects the Tissue Developmental Patterns of Human Mesenchymal Stem Cells in 3D Scaffolds. *J. Cell. Physiol.* **2009**, *219* (2), 421–429. https://doi.org/10.1002/JCP.21688.

(57) Lock, L. T.; Tzanakakis, E. S. Expansion and Differentiation of Human Embryonic Stem Cells to Endoderm Progeny in a Microcarrier Stirred-Suspension Culture. *Tissue Eng. - Part A* **2009**, *15* (8), 2051–2063. https://doi.org/10.1089/ten.tea.2008.0455.

(58) Schindelin, J.; Arganda-Carreras, I.; Frise, E.; Kaynig, V.; Longair, M.; Pietzsch, T.; Preibisch, S.; Rueden, C.; Saalfeld, S.; Schmid, B.; Tinevez, J. Y.; White, D. J.; Hartenstein, V.; Eliceiri, K.; Tomancak, P.; Cardona, A. Fiji: An Open-Source Platform for Biological-Image Analysis. *Nature Methods*. 2012, pp 676–682. https://doi.org/10.1038/nmeth.2019.

(59) Chen, C.; Loe, F.; Blocki, A.; Peng, Y.; Raghunath, M. Applying Macromolecular Crowding to Enhance Extracellular Matrix Deposition and Its Remodeling in Vitro for Tissue Engineering and Cell-Based Therapies. *Adv. Drug Deliv. Rev.* **2011**, *63* (4), 277–290. https://doi.org/10.1016/j.addr.2011.03.003.

(60) Lareu, R. R.; Subramhanya, K. H.; Peng, Y.; Benny, P.; Chen, C.; Wang, Z.; Rajagopalan, R.; Raghunath, M. Collagen Matrix Deposition Is Dramatically Enhanced in Vitro When Crowded with Charged Macromolecules: The Biological Relevance of the Excluded Volume Effect. *FEBS Lett.* **2007**, *581* (14), 2709–2714. https://doi.org/10.1016/j.febslet.2007.05.020.

(61) Hussey, G. S.; Keane, T. J.; Badylak, S. F. The Extracellular Matrix of the Gastrointestinal Tract: A Regenerative Medicine Platform. *Nature Reviews Gastroenterology and Hepatology*. Nature Publishing Group September 1, 2017, pp 540–552. https://doi.org/10.1038/nrgastro.2017.76.

(62) Martinez-Hernandez, A.; Amenta, P. S. The Hepatic Extracellular Matrix - II. Ontogenesis, Regeneration and Cirrhosis. *Virchows Archiv A Pathological Anatomy and Histopathology*. Springer-Verlag March 1993, pp 77–84. https://doi.org/10.1007/BF01606580.

(63) Genovese, F.; Manresa, A. A.; Leeming, D. J.; Karsdal, M. A.; Boor, P. The Extracellular Matrix in the Kidney: A Source of Novel Non-Invasive Biomarkers of Kidney Fibrosis? *Fibrogenesis and Tissue Repair*. BioMed Central Ltd. March 28, 2014, p 4. https://doi.org/10.1186/1755-1536-7-4.

(64) Ruoslahti, E. *Brain Extracellular Matrix*; 1996; Vol. 6.

(65) Gillies, A. R.; Lieber, R. L. Structure and Function of the Skeletal Muscle Extracellular Matrix. *Muscle Nerve* **2011**, *44* (3), 318. https://doi.org/10.1002/MUS.22094.

(66) Uitto, J.; Olsen, D. R.; Fazio, M. J. Extracellular Matrix of the Skin: 50 Years of Progress. *J. Invest. Dermatol.* **1989**, *92* (s4), 61S-77S. https://doi.org/10.1111/1523-1747.ep13075039.

(67) Hughes, C. S.; Postovit, L. M.; Lajoie, G. A. Matrigel: A Complex Protein Mixture

Required for Optimal Growth of Cell Culture. *Proteomics* **2010**, *10* (9), 1886–1890. https://doi.org/10.1002/pmic.200900758.

(68) Andreu, I.; Luque, T.; Sancho, A.; Pelacho, B.; Iglesias-García, O.; Melo, E.; Farré, R.; Prósper, F.; Elizalde, M. R.; Navajas, D. Heterogeneous Micromechanical Properties of the Extracellular Matrix in Healthy and Infarcted Hearts. *Acta Biomater.* **2014**, *10* (7), 3235–3242. https://doi.org/10.1016/j.actbio.2014.03.034.

(69) Nonaka, P. N.; Campillo, N.; Uriarte, J. J.; Garreta, E.; Melo, E.; De Oliveira, L. V. F.; Navajas, D.; Farré, R. Effects of Freezing/Thawing on the Mechanical Properties of Decellularized Lungs. *J. Biomed. Mater. Res. - Part A* **2014**, *102* (2), 413–419. https://doi.org/10.1002/jbm.a.34708.

(70) Ranamukhaarachchi, S. K.; Modi, R. N.; Han, A.; Velez, D. O.; Kumar, A.; Engler, A. J.; Fraley, S. I. Macromolecular Crowding Tunes 3D Collagen Architecture and Cell Morphogenesis. *Biomater. Sci.* **2019**, *7* (2), 618–633. https://doi.org/10.1039/c8bm01188e.

(71) Leiva, O.; Leon, C.; Kah Ng, S.; Mangin, P.; Gachet, C.; Ravid, K. The Role of Extracellular Matrix Stiffness in Megakaryocyte and Platelet Development and Function. *American Journal of Hematology*. Wiley-Liss Inc. March 1, 2018, pp 430–441. https://doi.org/10.1002/ajh.25008.

(72) Velling, T.; Risteli, J.; Wennerberg, K.; Mosher, D. F.; Johansson, S. Polymerization of Type I and III Collagens Is Dependent on Fibronectin and Enhanced by Integrins A11β1 and A2β1. *J. Biol. Chem.* **2002**, *277* (40), 37377–37381. https://doi.org/10.1074/jbc.M206286200.

(73) Butcher, D. T.; Alliston, T.; Weaver, V. M. A Tense Situation: Forcing Tumour Progression. *Nat. Rev. Cancer* **2009**, *9* (2), 108–122. https://doi.org/10.1038/nrc2544.

(74) Kutys, M. L.; Doyle, A. D.; Yamada, K. M. Regulation of Cell Adhesion and Migration by Cell-Derived Matrices. *Exp Cell Res.* **2013**, *319* (16), 2434–2439. https://doi.org/10.1016/j.yexcr.2013.05.030.Regulation.

(75) Ventre, M.; Coppola, V.; Natale, C. F.; Netti, P. A. Aligned Fibrous Decellularized Cell Derived Matrices for Mesenchymal Stem Cell Amplification. *J. Biomed. Mater. Res. Part A* **2019**, *107* (11), 2536–2546. https://doi.org/10.1002/jbm.a.36759.

(76) Harunaga, J. S.; Yamada, K. M. Cell-Matrix Adhesions in 3D Jill. *Matrix Biol.* **2011**, *30* (7), 363–3687. https://doi.org/10.1016/j.matbio.2011.06.001.

(77) Zeiger, A. S.; Loe, F. C.; Li, R.; Raghunath, M.; van Vliet, K. J. Macromolecular Crowding Directs Extracellular Matrix Organization and Mesenchymal Stem Cell Behavior. *PLoS One* **2012**, *7* (5). https://doi.org/10.1371/journal.pone.0037904.

(78) Shendi, D.; Marzi, J.; Linthicum, W.; Rickards, A. J.; Dolivo, D. M.; Keller, S.; Kauss, M. A.; Wen, Q.; McDevitt, T. C.; Dominko, T.; Schenke-Layland, K.; Rolle, M. W. Hyaluronic Acid as a Macromolecular Crowding Agent for Production of Cell-Derived Matrices. *Acta Biomater.* **2019**. https://doi.org/10.1016/j.actbio.2019.09.042.

(79) Benny, P.; Badowski, C.; Lane, E. B.; Raghunath, M. Improving 2D and 3D Skin <Em>In Vitro</Em> Models Using Macromolecular Crowding. *J. Vis. Exp.*

2016, No. 114, 1–11. https://doi.org/10.3791/53642.

(80) B, P.; MK, H.; VM, W. Fibrosis and Cancer: A Strained Relationship. *Biochim. Biophys. acta. Rev. cancer* **2020**, *1873* (2). https://doi.org/10.1016/J.BBCAN.2020.188356.

(81) Zhu, H.; Liu, Q.; Miao, L.; Musetti, S.; Huo, M.; Huang, L. Remodeling the Fibrotic Tumor Microenvironment of Desmoplastic Melanoma to Facilitate Vaccine Immunotherapy. *Nanoscale* **2020**, *12* (5), 3400–3410. https://doi.org/10.1039/C9NR09610H.

(82) Bauer, J.; Emon, M. A. B.; Staudacher, J. J.; Thomas, A. L.; Zessner-Spitzenberg, J.; Mancinelli, G.; Krett, N.; Saif, M. T.; Jung, B. Increased Stiffness of the Tumor Microenvironment in Colon Cancer Stimulates Cancer Associated Fibroblast-Mediated Prometastatic Activin A Signaling. *Sci. Reports 2020 101* **2020**, *10* (1), 1–11. https://doi.org/10.1038/s41598-019-55687-6.

(83) Emon, B.; Bauer, J.; Jain, Y.; Jung, B.; Saif, T. Biophysics of Tumor Microenvironment and Cancer Metastasis - A Mini Review. *Comput. Struct. Biotechnol. J.* **2018**, *16*, 279–287. https://doi.org/10.1016/J.CSBJ.2018.07.003.

(84) Farhane, Z.; Bonnier, F.; Howe, O.; Casey, A.; Byrne, H. J. Doxorubicin Kinetics and Effects on Lung Cancer Cell Lines Using in Vitro Raman Micro-Spectroscopy: Binding Signatures, Drug Resistance and DNA Repair. *J. Biophotonics* **2018**, *11* (1), e201700060. https://doi.org/10.1002/jbio.201700060.

(85) Lin, J.; Yu, Y.; Shigdar, S.; Fang, D. Z.; Du, J. R.; Wei, M. Q.; Danks, A.; Liu, K.; Duan, W. Enhanced Antitumor Efficacy and Reduced Systemic Toxicity of Sulfatide-Containing Nanoliposomal Doxorubicin in a Xenograft Model of Colorectal Cancer. *PLoS One* **2012**, *7* (11), 49277. https://doi.org/10.1371/journal.pone.0049277.

(86) Brauchle, E.; Kasper, J.; Daum, R.; Schierbaum, N.; Falch, C.; Kirschniak, A.; Schäffer, T. E.; Schenke-Layland, K. Biomechanical and Biomolecular Characterization of Extracellular Matrix Structures in Human Colon Carcinomas. *Matrix Biol.* **2018**, *68–69*, 180–193. https://doi.org/10.1016/j.matbio.2018.03.016.

(87) Johnson, L. A.; Rodansky, E. S.; Sauder, K. L.; Horowitz, J. C.; Mih, J. D.; Tschumperlin, D. J.; Higgins, P. D. Matrix Stiffness Corresponding to Strictured Bowel Induces a Fibrogenic Response in Human Colonic Fibroblasts. *Inflamm. Bowel Dis.* **2013**, *19* (5), 891–903. https://doi.org/10.1097/MIB.0b013e3182813297.

(88) Okuyama, H.; Kondo, J.; Sato, Y.; Endo, H.; Nakajima, A.; Piulats, J. M.; Tomita, Y.; Fujiwara, T.; Itoh, Y.; Mizoguchi, A.; Ohue, M.; Inoue, M. Dynamic Change of Polarity in Primary Cultured Spheroids of Human Colorectal Adenocarcinoma and Its Role in Metastasis. *Am. J. Pathol.* **2016**, *186* (4), 899–911. https://doi.org/10.1016/J.AJPATH.2015.12.011.

(89) Stylianopoulos, T.; Munn, L. L.; Jain, R. K. Reengineering the Physical Microenvironment of Tumors to Improve Drug Delivery and Efficacy: From Mathematical Modeling to Bench to Bedside. **2018**. https://doi.org/10.1016/j.trecan.2018.02.005.

(90) Slater, C.; De La Mare, J. A.; Edkins, A. L. In Vitro Analysis of Putative Cancer Stem Cell Populations and Chemosensitivity in the SW480 and SW620 Colon Cancer Metastasis Model. *Oncol. Lett.* **2018**, *15* (6), 8516–8526. https://doi.org/10.3892/ol.2018.8431.

(91) Biazik, J. M.; Jahn, K. A.; Su, Y.; Wu, Y. N.; Braet, F. Unlocking the Ultrastructure of Colorectal Cancer Cells in Vitro Using Selective Staining. *World J. Gastroenterol.* **2010**, *16* (22), 2743–2753. https://doi.org/10.3748/wjg.v16.i22.2743.

(92) Holle, A. W.; Young, J. L.; Spatz, J. P. In Vitro Cancer Cell-ECM Interactions Inform in Vivo Cancer Treatment. *Adv. Drug Deliv. Rev.* **2016**, *97*, 270–279. https://doi.org/10.1016/j.addr.2015.10.007.

(93) Sherman-Baust, C. A.; Weeraratna, A. T.; Rangel, L. B. A.; Pizer, E. S.; Cho, K. R.; Schwartz, D. R.; Shock, T.; Morin, P. J. Remodeling of the Extracellular Matrix through Overexpression of Collagen VI Contributes to Cisplatin Resistance in Ovarian Cancer Cells. *Cancer Cell* **2003**, *3* (4), 377–386. https://doi.org/10.1016/S1535-6108(03)00058-8.

(94) Naci, D.; El Azreq, M. A.; Chetoui, N.; Lauden, L.; Sigaux, F.; Charron, D.; Al-Daccak, R.; Aoudjit, F. A2β1 Integrin Promotes Chemoresistance against Doxorubicin in Cancer Cells through Extracellular Signal-Regulated Kinase (ERK). *J. Biol. Chem.* **2012**, *287* (21), 17065–17076. https://doi.org/10.1074/jbc.M112.349365.

(95) Levato, R.; Visser, J.; Planell, J. A.; Engel, E.; Malda, J.; Mateos-Timoneda, M. A. Biofabrication of Tissue Constructs by 3D Bioprinting of Cell-Laden Microcarriers. *Biofabrication* **2014**, *6* (3). https://doi.org/10.1088/1758-5082/6/3/035020.

(96) Shekaran, A.; Lam, A.; Sim, E.; Jialing, L.; Jian, L.; Wen, J. T. P.; Chan, J. K. Y.; Choolani, M.; Reuveny, S.; Birch, W.; Oh, S. Biodegradable ECM-Coated PCL Microcarriers Support Scalable Human Early MSC Expansion and in Vivo Bone Formation. *Cytotherapy* **2016**, *18* (10), 1332–1344. https://doi.org/10.1016/j.jcyt.2016.06.016.

(97) Rashid, R.; Lim, N. S. J.; Chee, S. M. L.; Png, S. N.; Wohland, T.; Raghunath, M. Novel Use for Polyvinylpyrrolidone as a Macromolecular Crowder for Enhanced Extracellular Matrix Deposition and Cell Proliferation. *Tissue Eng. Part C Methods* **2014**, *20* (12), 994–1002. https://doi.org/10.1089/ten.tec.2013.0733.

(98) Alcaraz, J.; Otero, J.; Jorba, I.; Navajas, D. Bidirectional Mechanobiology between Cells and Their Local Extracellular Matrix Probed by Atomic Force Microscopy. *Seminars in Cell and Developmental Biology*. Elsevier Ltd January 1, 2018, pp 71–81. https://doi.org/10.1016/j.semcdb.2017.07.020.